

© Copyright by Eduardo Hernández 2016
All Rights Reserved

**Optical Emission Diagnostics of a Non-equilibrium
Atmospheric Pressure Helium Plasma Jet in Ambient Air**

A Thesis

Presented to

the Faculty of the Department of Chemical & Biomolecular Engineering

University of Houston

In Partial Fulfillment

of the Requirements of the Degree

Master of Science

in Chemical Engineering

by

Eduardo Hernández

May 2016

**Optical Emission Diagnostics of a Non-equilibrium
Atmospheric Pressure Helium Plasma Jet in Ambient Air**

Eduardo Hernández

Approved:

Co-Chair of the Committee
Dr. Vincent M. Donnelly, Professor
Chemical & Biomolecular Engineering

Co-Chair of the Committee
Dr. Demetre J. Economou, Professor
Chemical & Biomolecular Engineering

Committee Members:

Dr. John C. Wolfe, Professor
Electrical & Computer Engineering

Dr. Suresh K. Khator, Associate Dean
Cullen College of Engineering

Dr. Michael P. Harold
Professor and Department Chairman
Chemical & Biomolecular Engineering

Acknowledgements

I would like to express my deepest gratitude to my master thesis advisors Dr. Vincent M. Donnelly and Dr. Demetre J. Economou for their guidance and recommendations. It has been a growing experience both personally and intellectually. I would like to also thank everyone in the Plasma Processing Laboratory at the University of Houston for their much appreciated input and long discussions. Finally, I want to recognize all my friends and particularly my parents for their unconditional support throughout my undergraduate and graduate studies.

**Optical Emission Diagnostics of a Non-equilibrium
Atmospheric Pressure Helium Plasma Jet in Ambient Air**

An Abstract

Of a

Thesis

Presented to

the Faculty of the Department of Chemical & Biomolecular Engineering

University of Houston

In Partial Fulfillment

of the Requirements of the Degree

Master of Science

in Chemical Engineering

by

Eduardo Hernández

May 2016

Abstract

Non-thermal atmospheric pressure plasmas are increasingly attracting more attention from the scientific community for their potential use in surface treatment and biomedical applications. Even though considerable progress has been made, investigation of the species generated at close proximity (1 mm to ~100 nm) to a surface has not been addressed due to limitations of common optical techniques. A novel approach using Optical Emission Spectroscopy (OES) that can probe emissions over this distance away from the surface has been investigated. Additionally, the presence of high energy VUV photons was confirmed and these can play an important role in the propagation of plasma jets. By performing temporally resolved OES, it was determined that excitation of O, N, OH, NO and N_2^+ is predominantly due to collisions between He^* and their precursors, whereas the N_2 emissions are due to electron impact that produces electronically excited N_2 .

Table of Contents

| | |
|--|------|
| Acknowledgements | v |
| Abstract | vii |
| Table of Contents | viii |
| List of Figures | x |
| List of Tables | xiii |
| Chapter 1: Introduction | 1 |
| Chapter 2: Literature Review | 3 |
| 2.1 Plasma Generation..... | 3 |
| 2.2 Low Pressure and Atmospheric Pressure Plasmas | 5 |
| 2.3 Atmospheric pressure plasma chemistry..... | 8 |
| 2.4 Refraction of Light..... | 10 |
| Chapter 3: Experimental Methods | 14 |
| 3.1 Experimental Apparatus | 14 |
| 3.2 Atmospheric Plasma Optical Emission Spectroscopy | 15 |
| 3.3 Time-resolved Plasma Jet Imaging and Spectroscopy..... | 16 |
| 3.4 Angular Time-resolved Optical Emission Spectroscopy | 18 |
| 3.5 Vacuum Ultraviolet Spectroscopy | 19 |
| Chapter 4: Results and Discussion..... | 23 |
| 4.1 Plasma Emission Characterization and Angular Spectroscopy..... | 23 |
| 4.2 Time-resolved Imaging and Spectroscopy..... | 27 |
| 4.3 UV/VUV to NIR Time-resolved Spectroscopy | 35 |

| | |
|---|----|
| Chapter 5: Summary and Conclusions..... | 45 |
| References..... | 47 |
| Appendix..... | 54 |

List of Figures

| | |
|--|----|
| Figure 1 Schematic of breakdown voltage for a gas between parallel plates. ^[11] | 5 |
| Figure 2 Variation of electron and gas temperature with pressure in a gas arc discharge. ^[12] | 6 |
| Figure 3 Refraction of light passing from medium 1 to medium 2, and generation of evanescent wave through total internal reflection. | 11 |
| Figure 4 Penetration depth for evanescent wave in air created by several common photons found in atmospheric plasmas undergoing TIR inside fused silica. | 12 |
| Figure 5 Plasma Jet configuration with ring electrodes. | 14 |
| Figure 6 Voltage amplifier circuit..... | 15 |
| Figure 7 Experimental apparatus. | 16 |
| Figure 8 ICCD triggering: The green signal, with the same frequency and in phase with the voltage powering the plasma, acts as a triggering signal for the ICCD controller. After some delay time, which can be controlled via software, the camera is activated (gated) and acquires signal for a set exposure time. | 17 |
| Figure 9 (a) Main parts of an ICCD camera and (b) amplification of a single electron. ... | 18 |
| Figure 10 Experimental apparatus for VUV spectroscopy. | 20 |
| Figure 11 (a) Circuitry for high voltage divider and (b) construction of photomultiplier tube. | 21 |
| Figure 12 Typical He atmospheric pressure plasma spectrum from 300 nm to 900 nm. ... | 23 |
| Figure 13 Typical helium atmospheric pressure plasmas spectrum from 200 to 300 nm. ... | 24 |
| Figure 14 Angular-resolved optical emission spectroscopy. | 26 |
| Figure 15 Atmospheric pressure plasma jet voltage-current plot. | 27 |

| | |
|--|----|
| Figure 16 Time along plasma voltage corresponding to when the images of Figure 17 were taken. | 28 |
| Figure 17 ICCD 10 ns exposure time images (false color) of helium atmospheric pressure plasma jet from (a)10-2000 ns and (b)2300-4500 ns. Corresponding times are shown on the voltage waveform of Figure 16. | 31 |
| Figure 18 Time-resolved He emission at various angles. Intensities of all but the 0° measurements are indicated by the left y-axis. | 33 |
| Figure 19 Position in time corresponding to time-resolved emissions. | 33 |
| Figure 20 Probing the region close to the prism surface. By collecting OES at 10°, 20°, and 30°, one is probing light from approximately 5.6, 2.6, and 0.35 mm away from the surface. | 34 |
| Figure 21 He atmospheric pressure plasma spectrum in the UV-VUV range. | 35 |
| Figure 22 Absorption of O 130.2 nm and N 149.2 VUV photons in air. | 37 |
| Figure 23 Absorption spectrum of O ₂ . ^[54] | 38 |
| Figure 24 Time resolved O 130.2 nm emission with plasma jet positioned (a) normal to the MgF ₂ window and (b) at some angle with respect to the surface. | 39 |
| Figure 25 Time resolved VUV emissions. | 40 |
| Figure 26 Time-resolved He (706 nm) and O (777 nm) emissions recorded with the ICCD camera. | 41 |
| Figure 27 Time resolved OH (306-309 nm) and N ₂ SPS (337 nm) emissions recorded with the ICCD camera. | 43 |

| | |
|---|----|
| Figure 28 Helium atmospheric pressure plasma spectrum (a) at the maximum of the applied voltage, (b) the minimum of the applied, and (c) at the zero crossing of the applied voltage..... | 44 |
| Figure 29 Typical He atmospheric pressure plasma spectrum from 100 nm to 900 nm. Peaks marked with II are those from second-order diffraction..... | 54 |
| Figure 30 Typical emission spectrum, exhibiting both N ₂ (blue) and N ₂ ⁺ (red) with corresponding vibrational quantum numbers v'-v". | 55 |

List of Tables

| | |
|---|----|
| Table 1 Parameters A and B for calculation of Townsend ionization coefficient. ^[9] | 4 |
| Table 2 Typical emitting species and transitions in He atmospheric pressure plasma jet emerging in air ambient. | 25 |
| Table 3 Typical emitting species and VUV transitions in He atmospheric pressure plasma jet emerging in air ambient. | 36 |
| Table 4 N ₂ and N ₂ ⁺ transitions in He atmospheric pressure plasma jet. | 55 |

Chapter 1: Introduction

Non-equilibrium (cold) atmospheric pressure plasmas are the subject of intense research due to their high potential for applications in different industries.^[1] This relatively immature technology has excited many researchers, including our group, to leap into this research area with the purpose of advancing the relevant science and technology by building upon the progress that has been made over the past 20 years.^[2]

Atmospheric pressure plasmas (APP) have a great advantage compared to the low-pressure plasmas used in the semiconductor industry, namely, APPs require no pumping systems. In addition, APPs need essentially no maintenance, are easy to build,^[1] and can be operated using both noble and molecular gases in either direct or alternate current mode.^[3] These nonthermal discharges, i.e., having a gas temperature close to room temperature and an electron temperature in excess of 10,000 K, provide a rich and reactive environment for surface treatment in areas like biomedicine and nanomaterials fabrication without damaging the substrate.^[1,5]

APP devices are relatively small and form a plasma inside a dielectric tube, often quartz. A plasma jet extends a small distance into air or any other ambient gas. This provides for a very localized treatment which has driven research in biomedicine, the most popular application for these plasmas.^[5] The potential of these plasmas in biomedicine is based on the reactive nitrogen and oxygen containing species that are often generated in the plasma and play an important role in biochemical processes. The source of these compounds is the ambient air or any other additives that can be mixed with the working gas or put in contact with the plasma jet.^[5]

Although atmospheric pressure low-temperature plasmas have been widely studied, measurements of fluxes and energies of species impacting on surfaces exposed to these plasmas are largely lacking. Further developments in biomedicine require such studies understanding the complex chemistry between living tissue and APPs. Specifically, understanding of the temporal evolution of VU/VUV radiation and reactive oxygen species is of paramount importance. To accomplish this, many researchers have performed optical emission spectroscopy (OES) but have been limited by the spatial resolution of up to a few μm .

This study pursued the use of a novel OES technique that could allow characterization of emissions generated by an APP at a distance of 1 mm to 100 nm away from the surface in contact with the plasma discharge. Additionally, detailed time-averaged and time-resolved UV/VUV-to-NIR optical emission spectroscopy of atmospheric pressure plasma was performed to gain a better understanding of the important role that high energy photons play in surface treatment using APPs and in the propagation of the plasma in air.

Chapter 2: Literature Review

2.1 Plasma Generation

A plasma is a gas composed of charged and neutral particles that exhibits collective behavior.^[6] The generation of vacuum and atmospheric pressure plasmas is based on the same principle. To ionize a gas, some type of energy, usually in the form of an electric field, must be fed into the gas. When in presence of a strong electric field, electrons are accelerated and can, in turn, collide with neutral atoms and molecules resulting in electron impact ionization.^[6] In addition, high energy photons produced by relaxation of excited species can help sustain the plasma through photoionization.^[8] This gas breakdown process is quite complicated but it is worth explaining. Plasma generation starts with a very small number of electrons that naturally exist in the ambient gas. A simple way to achieve breakdown of a gas is to have it exposed to a homogeneous electric field like that created by two parallel metal plates separated by a length d . Such electric field with strength V/d is then generated by applying a dc voltage between the plates:

$$E = V/d. \tag{1}$$

A free electron will then be accelerated in the direction opposite to the electric field. This electron can acquire enough energy from the field to be able to ionize a gas molecule and produce a new electron. The new electron can repeat this process resulting in an avalanche. This ionization process is called Townsend ionization and describes the electron production as a function of length in the electric field as

$$n_e(x) = n_{e0} \exp(x/\lambda) = n_{e0} \exp(\alpha x), \tag{2}$$

where λ is the mean free path for ionization and α is the Townsend ionization coefficient described as

$$\alpha = Ap \exp\left(\frac{-Bp}{E}\right), \quad (3)$$

where A and B are properties of the gas and are found in Table 1. The pressure term arises from the mean free path which is inversely proportional to the pressure (i.e., the amount of molecules or atoms encountered by the electrons).^[9]

Table 1 Parameters A and B for calculation of Townsend ionization coefficient.^[9]

| Gas | A ($cm^{-1}Torr^{-1}$) | B ($V cm^{-1}Torr^{-1}$) | Gas | A ($cm^{-1}Torr^{-1}$) | B ($V cm^{-1}Torr^{-1}$) |
|----------------|------------------------------------|--------------------------------------|------------|------------------------------------|--------------------------------------|
| Air | 15 | 365 | Ne | 4 | 100 |
| N ₂ | 10 | 310 | Ar | 12 | 180 |
| He | 3 | 34 | Kr | 17 | 240 |

Considering the differential form of equation (2),

$$\frac{dn_e}{dx} = \alpha n_e \quad (4)$$

n_{e0} initial electrons will produce

$$\alpha n_{e0} \exp(\alpha x) dx \quad (5)$$

number of ions in the slab in a differential thickness dx at a position x . Across the gap there will be $n_{e0}(\exp(\alpha d) - 1)$ ions. This current that propagates along the gap is self-sustained if

$$n_{e0} = \gamma n_{e0} (\exp(\alpha d) - 1) \quad (6)$$

or

$$\alpha d = \ln\left(1 + \frac{1}{\gamma}\right). \quad (7)$$

Equation (1) can be further developed by combining equations (2), (3) and (7) giving rise to Paschen's law:

$$V_b = \frac{Bpd}{\ln(Apd) - \ln(\ln(1 + \gamma^{-1}))}, \quad (8)$$

which allows for calculation of the breakdown voltage as a function of pressure, distance and working gas. Figure 1 shows how the voltage needed to ionize a gas between two electrodes increases with pressure; and goes to infinity as pressure decreases.^[11,12]

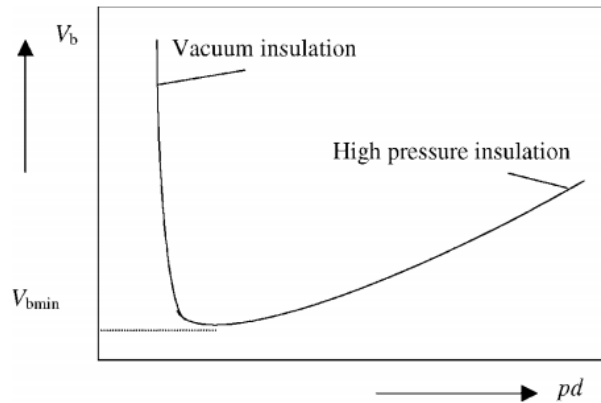


Figure 1 Schematic of breakdown voltage for a gas between parallel plates.^[11]

2.2 Low Pressure and Atmospheric Pressure Plasmas

Low pressure plasmas have been widely used in materials processing, specifically in the manufacture of semiconductor devices. For example, during the etching stage of manufacturing an integrated circuit, ions generated inside the plasma chamber are directionally accelerated towards the previously patterned substrate to etch away a specific amount of material forming very small features. Maintenance of a vacuum

plasmas system can be expensive and time consuming, disadvantages that are not applicable to atmospheric pressure plasmas.

Low-pressure plasmas have a lower gas temperature compared to the electron temperature. This arises from the inelastic collisions between electrons and other species, which sustain the discharge at low pressures without substantially raising the gas temperature. On the contrary, an increase in pressure will create more inelastic and elastic collisions between the species present in the ionized gas, with the latter being responsible for increasing the gas temperature (see Figure 2). Nonetheless, a low plasma (gas) temperature can be achieved at atmospheric pressures which brings up the necessity to differentiate thermal (equilibrium) and non-thermal plasmas.^[1]

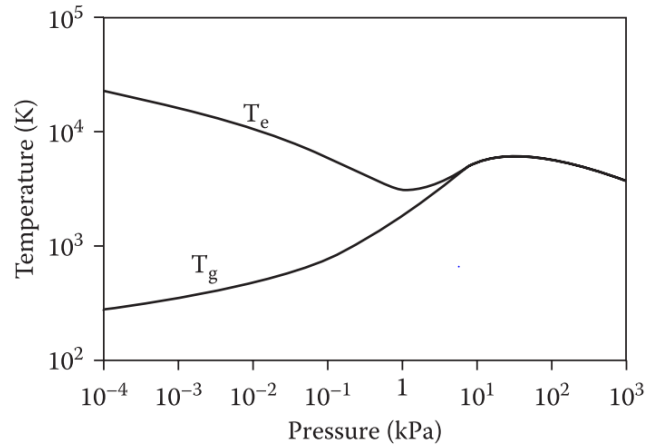


Figure 2 Variation of electron and gas temperature with pressure in a gas arc discharge.^[12]

The generation of non-thermal APPs can occur when the product of the characteristic length L and gas number density N is kept constant between the APPs and their low pressure counterparts. This requires that APPs have a small size (mm or below).

The applied power density also plays a role. By increasing the applied power, a cold APP may revert to an equilibrium plasma.^[1]

The types of atmospheric-pressure plasmas in this thesis are commonly referred to as atmospheric pressure plasma jets (APPJ) generated by flowing a noble gas often times with admixtures of reactive gases such as O₂ through a small dielectric tube.^[13] Others have generated plasmas using N₂^[15, 16] or air^[17, 18] as a working gas, even though these types of plasmas are harder to ignite and sustain. Frequently, generation of APPJs is achieved by placing two electrodes wrapped around the capillary tube and applying a high voltage across the electrodes to create the strong electric field needed to breakdown the gas. This configuration is referred to as a dielectric barrier discharge (DBD) jet. Other configurations have also been explored and are increasingly becoming popular in the field of plasma medicine.^[18] Most DBD jet devices can generate non-equilibrium plasmas with either kHz ac power or pulsed dc power with voltages ranging from a few kV to 30 kV and higher.^[19-20]

Plasma jets may appear continuous to the naked eye, but in fact, Teschke et al.^[20] and Lu et al.^[21] used fast imaging techniques and showed that what seemed to be continuous, were fast moving structures of ionized gas referred to as “plasma bullets”. They concluded that these structures were moving with velocities of 15 km/s to 150 km/s respectively. In general, such luminous fronts move with velocities in the order of 1-10,000 km/s.^[3, 24] Comparing the bullet velocity to the gas velocity and the drift velocity of the electrons, one can conclude that the bullet propagation in air was based on photoionization. The guiding of this ionization wave, commonly referred to as streamer, can be explained by the lower electric field required for helium ionization compared to

nitrogen or air. In addition, preionization of accumulated excited species from the preceding streamers may play a significant role.^[13]

2.3 Atmospheric pressure plasma chemistry

As mentioned earlier, non-equilibrium atmospheric pressure plasmas have low gas temperature which makes them ideal for biomedical applications.^[1,5] In particular, APPJs are the subject of intense investigations due to their promising applications in dentistry, sterilization, and even cancer treatment.^[25–27] It is clear that species commonly found in APPs, specifically reactive oxygen species (ROS) and reactive nitrogen species (RNS) play an important role in biology and medicine. Under just the right amounts, ROS and RNS can promote essential biological processes that help organisms fight diseases. However, under excessive amounts, they can lead to ‘oxidative stress’ which causes degradation of essential molecules in the cells.^[28, 29] Some of the most common ROS include ozone (O_3), hydrogen peroxide (H_2O_2), metastable oxygen ($*O_2$), and hydroxyl radical ($\bullet OH$). Common RNS include nitric oxide ($\bullet NO$) and nitrogen dioxide radical ($\bullet NO_2$). For a more comprehensive list and their specific roles see ref. 29.

Quite a few studies have used optical emission spectroscopy (OES) to monitor different species generated along the plasma jet. Emission intensities from different species depend on several factors such as: applied voltage, electrode configuration, and gas flow rate.^[30, 31, 32, 33] The gas composition is perhaps the most important parameter that ultimately establishes the characteristics of the plasma. It has been shown that the length of the plasma plume ensuing from the tube increases as a function of flow rate within the laminar regime. Once the Reynolds number reaches the transition regime, the

length of the plasma jet drops dramatically and then remains mostly constant under the turbulent regime.^[30] Performing OES as a function of position can be easily done and provides an estimate of the relative number density of species present as a function of position along the jet's axis.

Electron density and electron energy distributions can also be determined using OES. These plasma parameters are crucial in determining the capability of these plasmas in producing a flux of radicals and other reactive species that give the plasma discharge its characteristics.^[33] The most widely used technique for determining electron density in a high density plasma is Stark broadening of the hydrogen Balmer series atomic lines.^[3, 35, 36] Stark broadening occurs due to Coulomb interactions between the emitter and charged particles surrounding it, which partially breaks the degeneracy of atomic levels which in turns leads to what is known as the Stark effect. As a result of the Stark effect, the line shape, width, and position of the spectral line changes depending on the electron density and temperature. Electron densities, of the order 10^{14} - 10^{16} cm^{-3} ^[36] were estimated using hydrogen series lines. Stark broadening using the hydrogen Balmer series is considered the most reliable method to measure electron densities. Additionally, accurate plasma gas temperatures can be determined from the spectral region of about 300-490 nm that corresponds to the N₂ Second Positive System with the (0-0) transition being the most widely used due to its high intensity and the fact that it is free of interference with other spectral lines. The population density of these rotational levels obeys the Boltzmann distribution allowing for a theoretical fitting of an experimental spectrum of this region.^[37-39] The rotational temperature derived from the fitting of this N₂ spectrum is considered a good estimation of the kinetic temperature of the heavier

particles present in the plasma, i.e., gas temperature under high pressure conditions. Other molecular band systems like that of OH (A-X) and O₂ have also been used to estimate the gas temperature.^[39]

The effect of UV and VUV photons is less clear and is also addressed in this study. The presence of UV/VUV photons has proven to have enhanced deactivation of *B. subtilis* and *E. coli* bacteria by chemistry driven by ROS.^[40–42] VUV have the ability to excite gas phase species and to modify the surface being treated with these plasmas.

2.4 Refraction of Light

The interaction of light with matter has long been studied but it was Augustin-Jean Fresnel that developed the equations that described the behavior of electromagnetic waves of light passing through two different materials. When light in medium 1 with an index of refraction n_1 is incident with an angle θ_1 with respect to the normal on medium 2 with an index of refraction n_2 , where $n_1 > n_2$, light is refracted at an angle θ_2 which is smaller than θ_1 (see Figure 3). This process is described by

$$n_1 \sin(\theta_1) = n_2 \sin(\theta_2). \quad (9)$$

Total internal reflection (TIR) will occur in medium 1 when $\theta_2 > 90^\circ$, or when

$$\theta_2 > \text{asin}\left(\frac{n_2}{n_1}\right) = \theta_c \quad (10)$$

which introduces what is called the critical angle.^[43] Still, some of the energy endures and penetrates the other medium in the form of an evanescent wave (EW) as depicted in Figure 3.

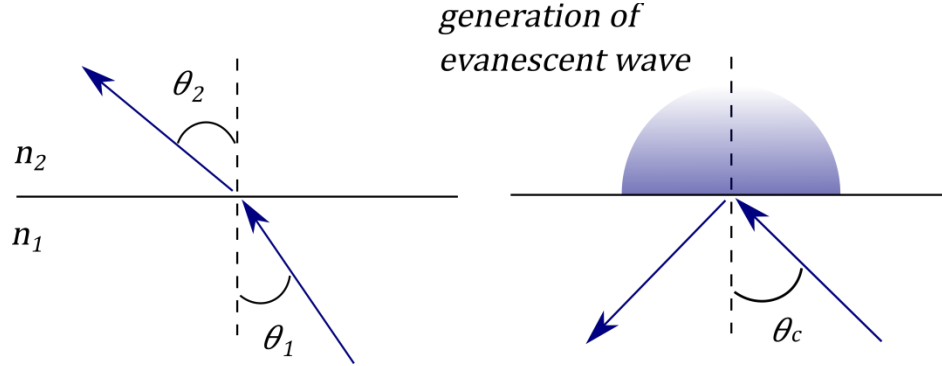


Figure 3 Refraction of light passing from medium 1 to medium 2, and generation of evanescent wave through total internal reflection.

This evanescent wave propagates only a few hundred nanometers into the second medium. The penetration depth, d_p , depends on the wavelength of the light wave that creates the evanescent wave, the angle between the normal and the plane of incidence, and the index or refraction of media 1 and 2.^[44] The relevant equation is,

$$d_p = \frac{\lambda}{2\pi(n_1^2 \sin(\theta)^2 - n_2^2)^{0.5}} \quad (11)$$

As the angle θ approaches the critical angle the penetration depth approaches infinity. As the angle is further increased, the penetration depth is greatly diminished as shown in Figure 4 at wavelengths for some common emissions present in atmospheric pressure helium plasma.

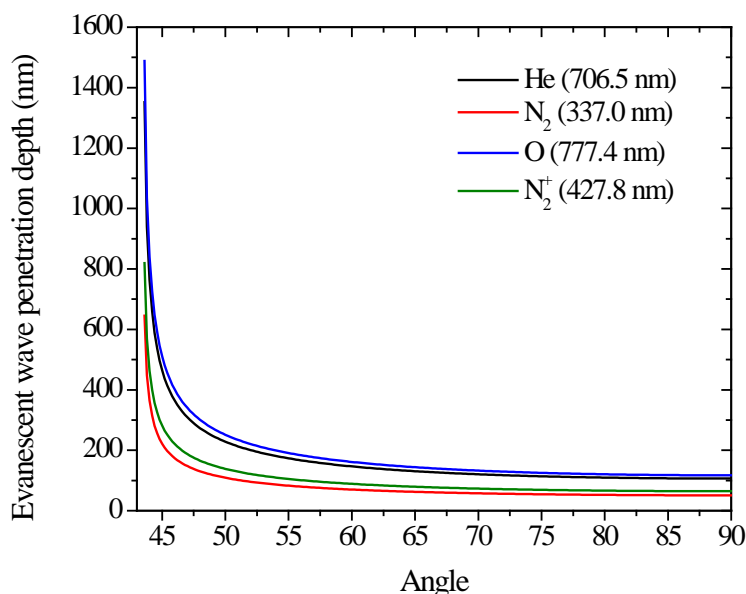


Figure 4 Penetration depth for evanescent wave in air created by several common photons found in atmospheric plasmas undergoing TIR inside fused silica.

Evanescent wave light has been used in the past as a method to image and study single molecules in solution at an interface.^[42, 45, 46] Less known, Evanescent wave light undergoing TIR can also excite emission in an adsorbate on a surface. Carniglia et al.^[45] demonstrated this by coating a glass slide with a 45 nm thick fatty acid layer doped with a fluorescent dye. Using an Ar⁺ laser, an evanescent wave was created at the glass-fatty acid interface by directing light at an angle larger than the critical angle. Emission from the dye was detected as a result Ar⁺ laser evanescent wave excitation.

Even more interesting, the reciprocal case was also determined to be true. A fluorescent layer at an interface excited by light can also create an evanescent wave which then propagates into the other medium as homogeneous light. This was confirmed by Carniglia et al.,^[45] when the fatty acid-dye layer was excited with Ar⁺ light and fluorescence was detected at angles exceeding the critical angle.

One motivation for this project is therefore the idea that if a species emits light from within a volume of an evanescent wave in a medium, some of that light is coupled into evanescent wave light, and thus homogeneous light can be detected inside the other medium at angles exceeding the critical angle. This method would allow us to determine, by OES, the species present in a region very close to the surface (~100 nm) interrogated by an atmospheric plasma jet. In addition, by selecting light on the normal incidence side of the critical angle, it is also possible to probe, integrated over distances of within 1 mm away from the surface, to the entire plasma stretching from inside the discharge tube to very near the surface. Finally, studying the time-dependent generation of VUV light and its penetration through air to the surface was a goal of this work.

Chapter 3: Experimental Methods

3.1 Experimental Apparatus

A variety of configurations of APPJs have been reported by different researchers using different configurations of electrodes.^[47] In this investigation, two different configurations were used to explore the ease of achieving uniform and stable plasma. The first set-up (see Figure 6) consisted of a grounded outer electrode and a powered internal electrode with a power feedthrough supplied through a Teflon tee. The discharge was generated in a quartz tube (5.5 mm ID and 9.5 mm OD) with a He (99.999% purity) gas flow of 4 L/min. The inner electrode was a thin copper rod, covered with a dielectric material, and positioned along the axis of the quartz tube. The ground ring electrode was positioned 5 mm from the edge of the tube.

The other arrangement consisted of a glass tube with the two ring electrodes wrapped around and separated by 15 mm. This arrangement produced a longer and more stable plasma jet. The position of the grounded electrode with respect to the high voltage electrode determines the direction of the plume as shown in Figure 5.

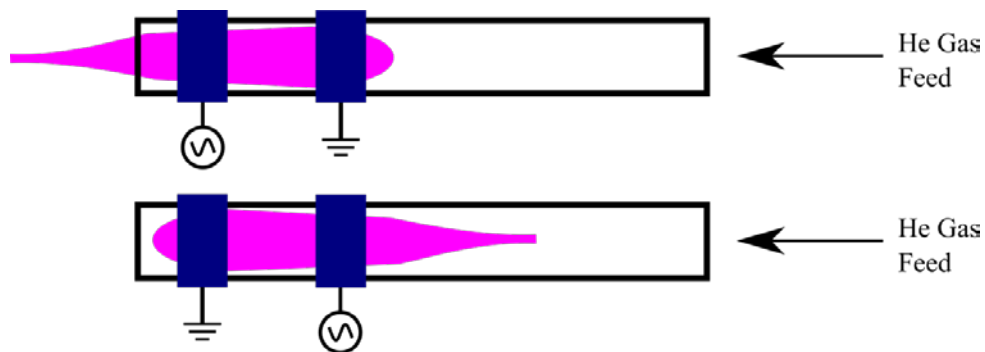


Figure 5 Plasma Jet configuration with ring electrodes.

The plasma was ignited by using high voltage RF power. A function generator supplied a sine wave with a voltage of $760 \text{ mV}_{\text{p-p}}$ at a frequency of 208 kHz. This output was fed into an RF amplifier and a home-made voltage amplifier L-C (inductor-capacitor) (Figure 6) to produce a voltage high enough to generate plasma. A high voltage probe (Tektronix 1000x attenuation) and an oscilloscope (Agilent Technologies DSO-X-2024A) were used to observe the voltage waveform supplied to the electrode.

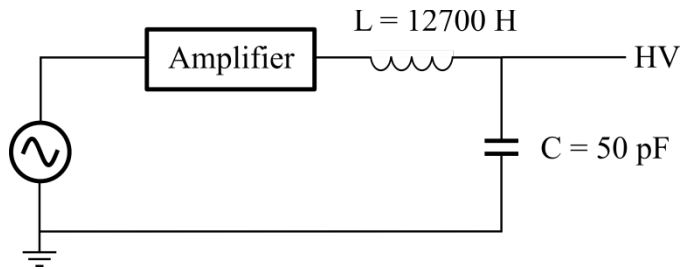


Figure 6 Voltage amplifier circuit.

3.2 Atmospheric Plasma Optical Emission Spectroscopy

The plasma plume was characterized using spectrometers (Ocean Optics model HR4000) with an optical fiber rated for wavelengths ranging from 200-1200 nm. Four different spectrometers were used to cover the full range of wavelengths from 200-900 nm. The flow rate was kept at 4.0 L/min with a fixed applied voltage on the electrode as specified in the previous section. The apparatus shown in Figure 7, consisted of a six-sided stainless steel chamber with a plano-convex (half cylinder prism) S1-UV fused silica lens on one of the chamber windows with the plasma jet impinging on the flat surface of the prism. Gas additives were not used during any of the experiments and the chamber ports were kept open to allow the free flow of ambient air.

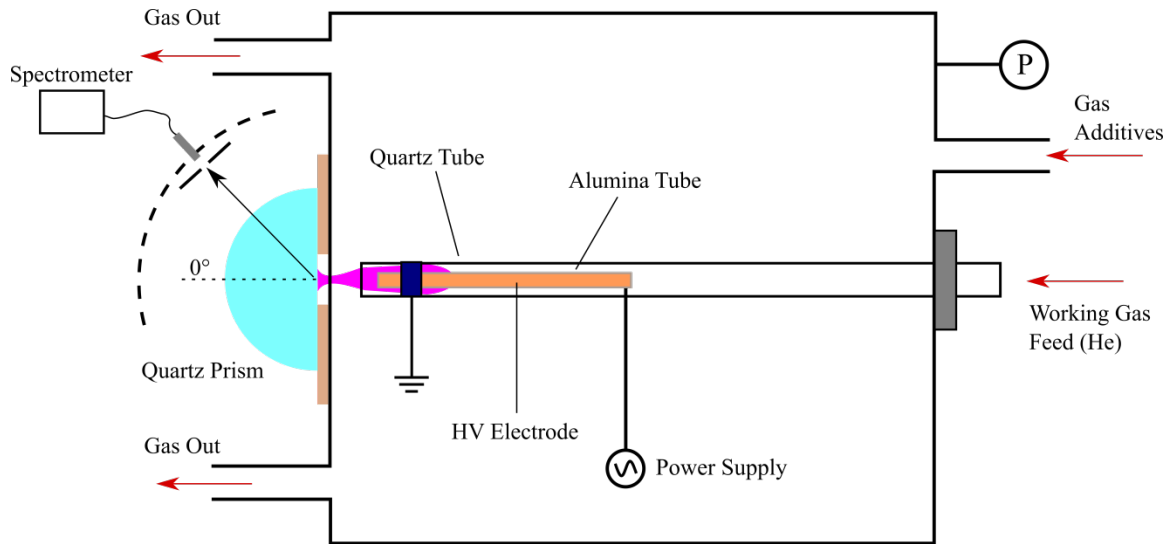


Figure 7 Experimental apparatus.

Light exiting the prism was collected by an optical fiber and coupled into one of the four spectrometers for a specific range of the spectrum. A 2.0 mm aperture was placed between the optical fiber and the prism to prevent any scattered or unwanted light from being detected. The optical fiber and aperture were both carefully aligned using a laser to “look” at the area where the plasma jet impinged the surface of the prism. An adjustable rotary stage with a precision of 2° permitted the movement of the optical fiber to different angles.

3.3 Time-resolved Plasma Jet Imaging and Spectroscopy

The dynamic nature of atmospheric plasma jets has been studied before. ^[21, 23, 24] Still, it was investigated to have a better understanding of the behavior of our atmospheric plasma source. To achieve this, a high-speed camera or an intensified CCD (Princeton Instrument PI-1024) and a plano-convex optical lens were used to take images of the plasma jet which it is known to evolve over the RF power period. The camera was

gated for a 10 ns duration over the voltage waveform and was accumulated over 12,000 periods to get a clear image. The intensity had to be accumulated over several cycles since 10 ns was a very short exposure time for the camera to obtain a significant amount of photons and show a clear image. The instant at which the camera acquired signal was changed using a delay generator. The timing and gating of the ICCD are shown in Figure 8.

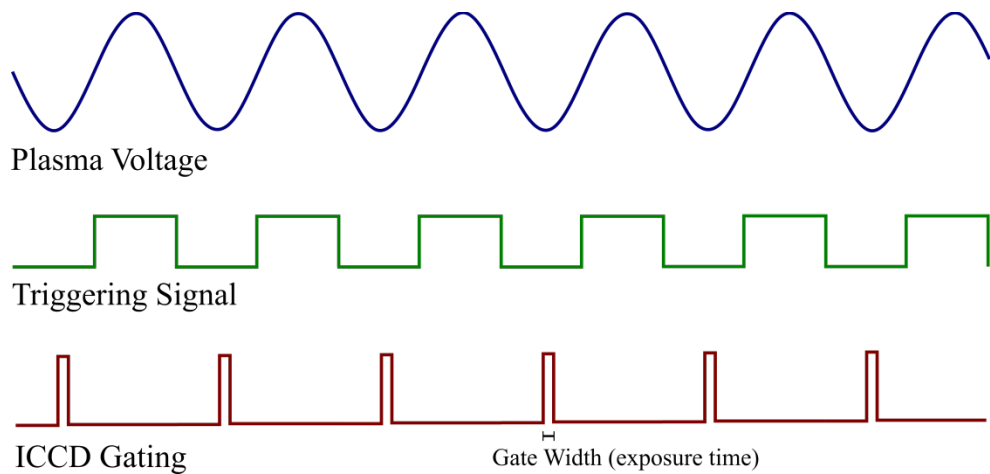


Figure 8 ICCD triggering: The green signal, with the same frequency and in phase with the voltage powering the plasma, acts as a triggering signal for the ICCD controller. After some delay time, which can be controlled via software, the camera is activated (gated) and acquires signal for a set exposure time.

An ICCD is much like a conventional CCD camera but it is able to intensify the image projected onto the photocathode.^[48] The main parts of an ICCD camera are shown in Figure 9. When a photon passes through the input window and strikes the photocathode, a photoelectron is emitted, which is then accelerated through the micro-channel plate by a strong electric field. This micro-channel plate is a thin disk with a honeycombed glass with thin channels. Once an electron enters the channel it is accelerated and successively hits the walls creating secondary electrons which then exit

the plate as a cloud of electrons traveling in a straight line with a resultant amplification as high as 10,000. The electron packet then hits the phosphor screen on the inside of a fiber optic exit window. The phosphor screen converts the electrons back to photons which are then coupled to the CCD using a fused fiber-optic bundle from the output of the image intensifier to the front side of the CCD window. This image is then digitalized and shown to the user as in a regular CCD camera. This ICCD is capable of intensifying very low levels of light due to short exposure time or a weak light source.

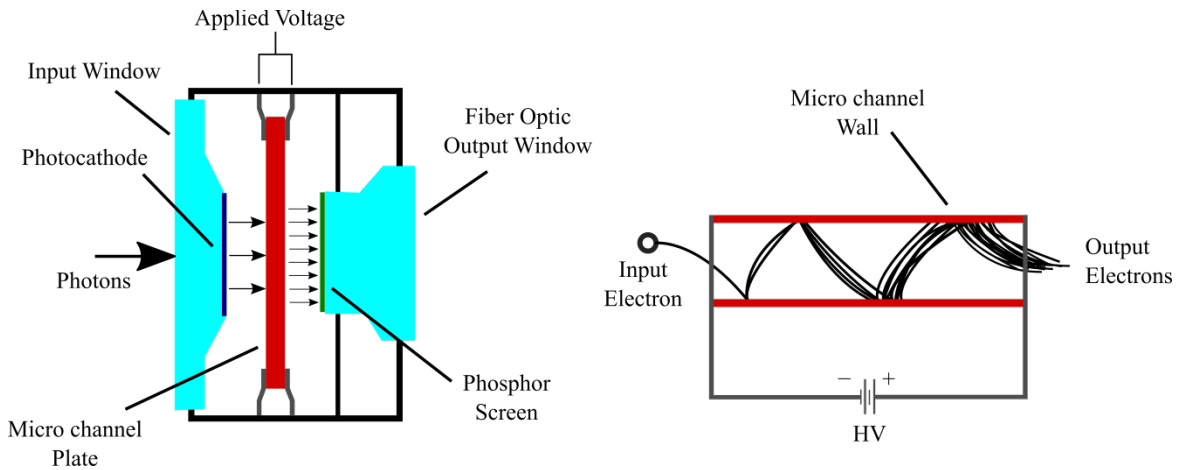


Figure 9 (a) Main parts of an ICCD camera and (b) amplification of a single electron.

These types of cameras are capable of rapidly gated at high frequencies and for a small period of time which enables them to capture, with great efficacy, an event lasting a few nanoseconds.

3.4 Angular Time-resolved Optical Emission Spectroscopy

The same ICCD camera used for imaging the atmospheric plasma jet was also used to time-resolved emissions coming from the plasma plume. It was mounted onto the exit port of a spectrometer (model Triax 550 from Horiba) with a 600 grooves/mm

grating. Using the same apparatus shown in Figure 7 and lens at the free end of the optical fiber, the light was focused onto the entrance slit of the spectrometer in order to perform the angular time-resolved measurements. The same methodology was followed of triggering the ICCD at different phases within the applied voltage waveform as for the imaging experiment. One complete trace consisted of 300 scans accumulated on the CCD (each with an exposure time of 50 ns) and was averaged over 500 acquisitions to reduce noise.

3.5 Vacuum Ultraviolet Spectroscopy

The role that vacuum ultraviolet (VUV) photons have in generating other species, sustaining the plasma by photoionization, and irradiating surfaces motivated the use of VUV spectroscopy to identify high energy photon emissions, and study their production mechanisms. The experimental apparatus used was a McPherson (Model 234/302) spectrometer equipped with a photomultiplier tube (PMT). The PMT had a sodium salicylate scintillator window attached to the PMT window that enabled detection of photons with wavelengths below 200 nm. The spectrometer was evacuated by a turbomolecular pump (TMP) backed by a roughing pump to achieve the low pressure ($\sim 10^{-7}$ Torr) required for detection of VUV photons. A magnesium fluoride window was placed in front of the entrance slit of the spectrometer and the plasma jet was positioned in front of this window as shown in Figure 10. This allowed for VUV photons to pass through the MgF_2 window, which has a cutoff wavelength of 120 nm (50 % transmission), and be detected by the photomultiplier.

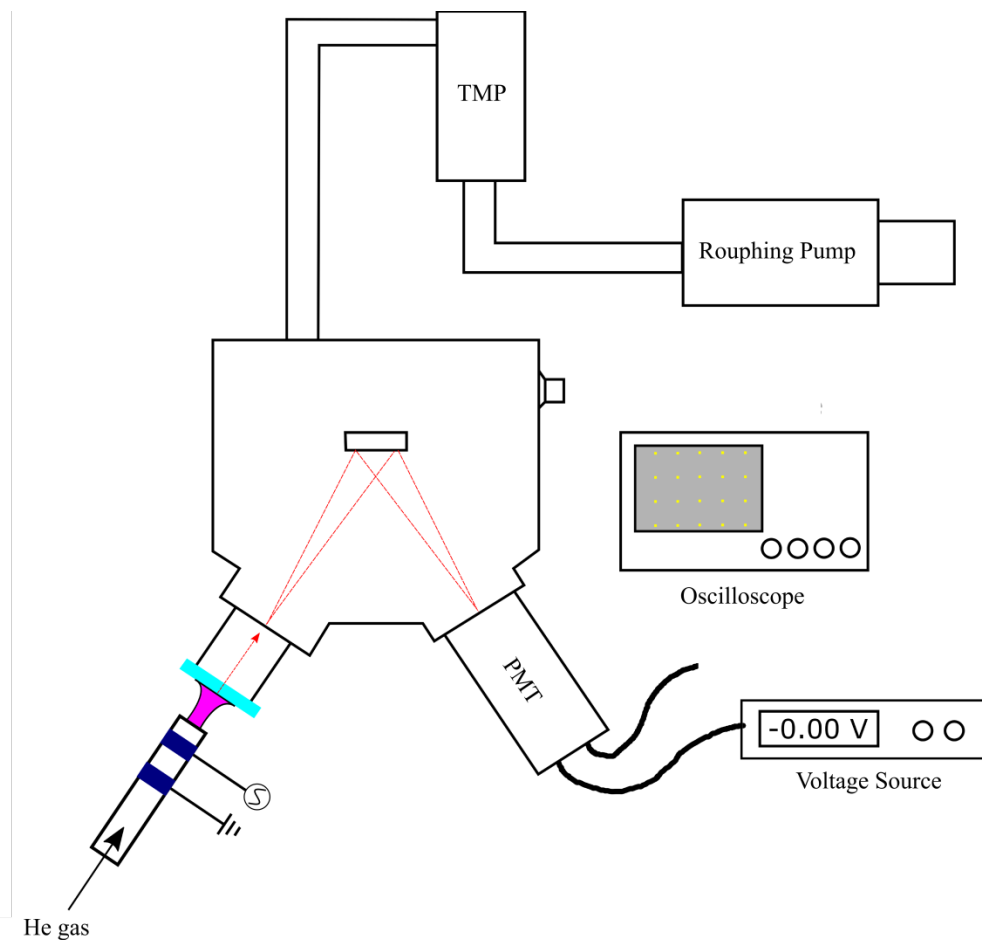


Figure 10 Experimental apparatus for VUV spectroscopy.

The working principle of a PMT is very similar to that of an ICCD in that they both convert light into an electrical signal and then amplify that signal to a useful level by emission of secondary electrons. The basic parts of PMT and its electrical circuit can be found in Figure 11.^[49]

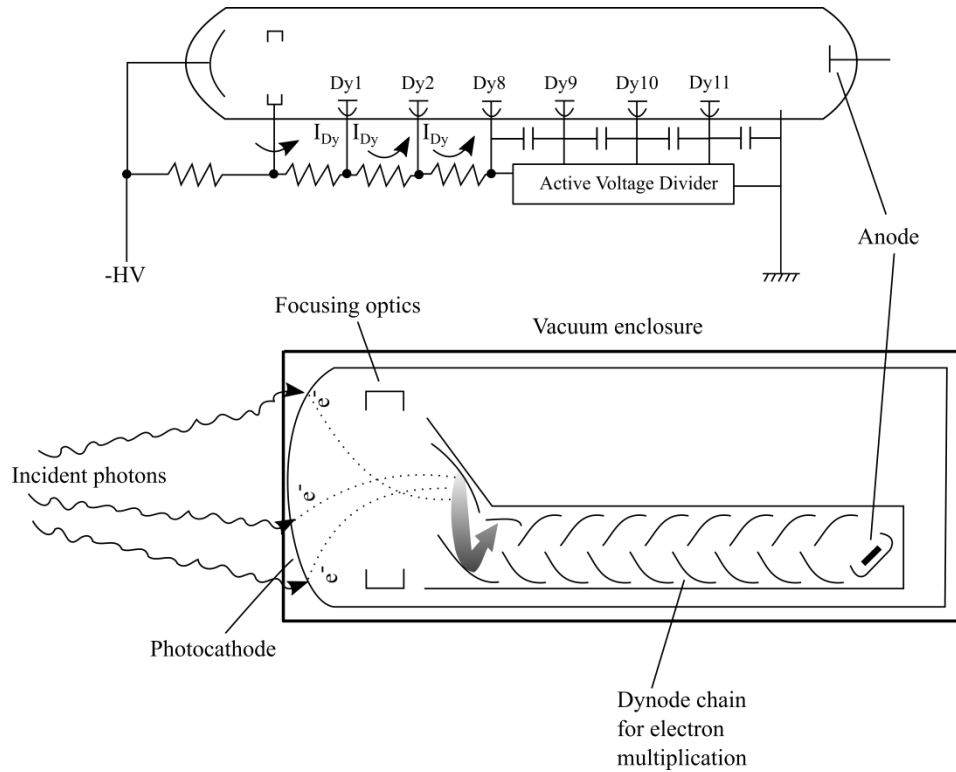


Figure 11 (a) Circuitry for high voltage divider and (b) construction of photomultiplier tube.

After a photon hits the photocathode, the electron that is generated passes by the focusing electrode and is driven by a strong electric field impacting the first dynode. The dynode releases secondary electrons which are then multiplied even further in every dynode, creating a cascade of electrons that are finally collected at the anode. Figure 11(a) shows the circuitry, serving as a voltage divider, capable of distributing a high negative voltage needed for the high electric field that drives the electrons from cathode to anode. The output signal from the PMT was either digitalized and then analyzed using LabView to acquire VUV spectra or passed through a 1 k Ω resistor and put into an oscilloscope to acquire time resolved measurements. The signal was then averaged over three minutes using the averaging function of the oscilloscope to get a time-resolved emission profile.

However, since the signal was very weak, a more appropriate technique based on photon counting was used to analyze the signal.

This photon counting technique is recommended to detect very low light levels in spectroscopic applications. A square wave synched to the same frequency of the RF voltage powering the plasma was used to trigger an oscilloscope and record the output from the photomultiplier. A photon counting technique uses a voltage threshold to discriminate between noise (seen as low amplitude spikes) and the signal that shows up as more intense spikes.

All spikes with values below the selected threshold of 0.04 mV were considered noise and therefore discarded, while spikes with values above 0.04 mV were counted as single photons striking the photocathode. The phase of these spikes, i.e., their time with respect to the voltage applied to the plasma, was recorded. By adjusting the time scale on the oscilloscope, 10 full periods of the RF power were captured. This permitted us to determine at what time a predominant amount of photons are emitted by the plasma. The data was averaged over 12,000 scans.

Chapter 4: Results and Discussion

4.1 Plasma Emission Characterization and Angular Spectroscopy

The high voltage RF power generated a plasma jet with a diameter of about 2 mm extending 1.2 cm in air and spreading over the surface of the prism over a small area (approx. 5 mm in diameter). A typical spectrum, Figure 7, taken at 0° with respect to the jet axis, revealed a variety of species present in the plasma. Full spectra covering the UV-NIR region of the He plasmas are shown in Figures 12 and 13.

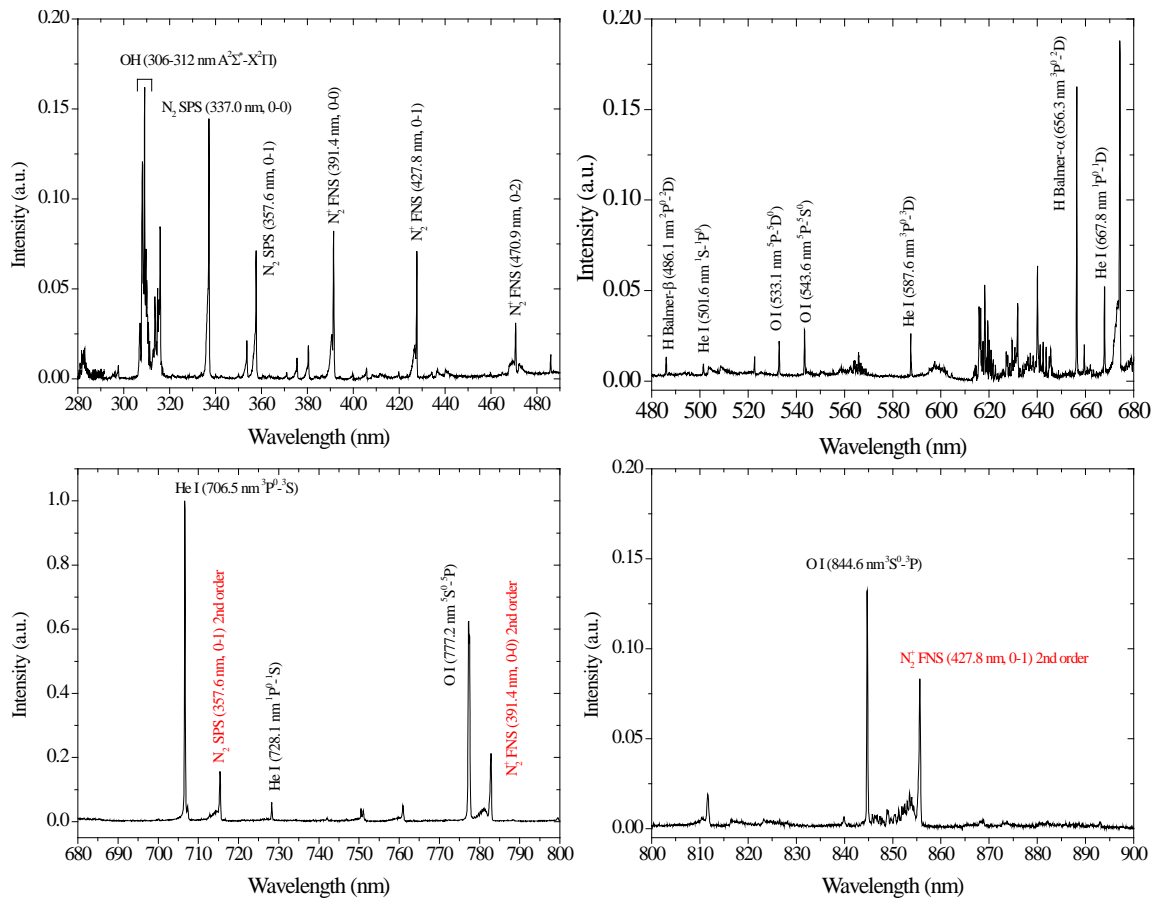


Figure 12 Typical He atmospheric pressure plasma spectrum from 300 nm to 900 nm.

Performing OES at 0 degrees with respect to the surface normal allows for photons generated along the plasma jet and also inside the quartz tube to enter the optical fiber and be detected by the spectrometers.

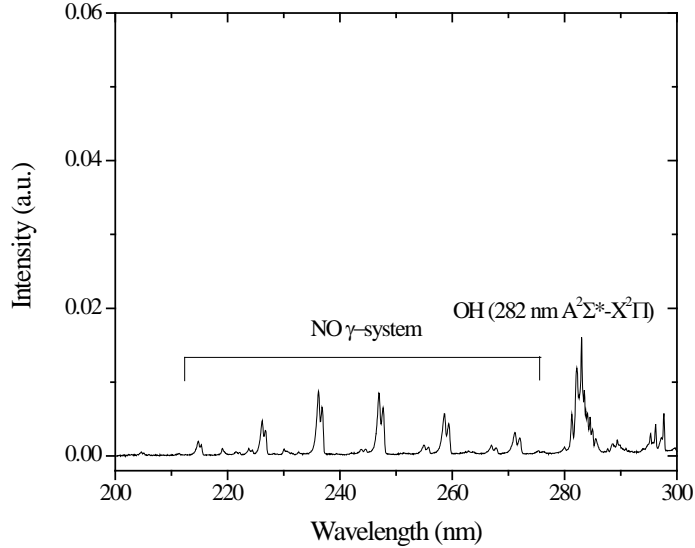


Figure 13 Typical helium atmospheric pressure plasmas spectrum from 200 to 300 nm.

The lower end of the spectrum is mostly dominated by OH ($A^2\Sigma^+ \rightarrow X^2\Pi$) emissions and different molecular nitrogen emissions including the N_2 ($C^3\Pi_u \rightarrow B^3\Pi_g$) second positive system (SPS) ranging from 300 – 380 nm. The N_2^+ ($B^2\Sigma_u^+ \rightarrow X^2\Sigma_g^+$) first negative system (FNS) is detected from 390 to 480 nm. Additionally, weak NO emission bands are observed ranging from 200 to 280 nm as shown in Figure 13. At higher wavelengths, He I transitions are detected, with 706.5 nm ($2p^3P^0 \rightarrow 3s^3S$) being the most intense line. Atomic oxygen emissions are also detected at 777.4 nm ($3s^5S^0 \rightarrow 3p^5P$) and 844.6 nm ($3s^3S^0 \rightarrow 3p^3P$). Table 2 shows the most noticeable transitions and energies in the UV-IR regions. Peaks marked in red were determined to be those from second-order

diffraction by using the appropriate long-wavelength-pass filters. Appendix A contains more detailed identifications of the transitions from the N_2 and N_2^+ .

Table 2 Typical emitting species and transitions in He atmospheric pressure plasma jet emerging in air ambient.

| Emitting species | Transition (de-excitation) | λ (nm) | E_{Lower} (eV) | E_{Upper} (eV) |
|-------------------------|---|----------------------------------|---|---|
| He I | $3p^1P^0 \rightarrow 2s^1S$ | 501.6 | 20.61 | 23.09 |
| He I | $3d^3D \rightarrow 2p^3P^0$ | 587.6 | 20.96 | 23.07 |
| He I | $3d^1D \rightarrow 2p^1P^0$ | 667.8 | 21.22 | 23.07 |
| He I | $3s^3S \rightarrow 2p^3P^0$ | 706.5 | 20.96 | 22.72 |
| He I | $3s^1S \rightarrow 2p^1P^0$ | 728.1 | 21.22 | 22.92 |
| H- α | $3d^2D \rightarrow 2p^2P^0$ | 656.3 | 10.20 | 12.09 |
| H- β | $4d^2D \rightarrow 2p^2P^0$ | 486.1 | 10.20 | 12.75 |
| O I | $5d^5D^0 \rightarrow 3p^5P$ | 533.1 | 10.74 | 13.06 |
| O I | $6s^5S^0 \rightarrow 3p^5P$ | 543.6 | 10.74 | 13.02 |
| O I | $3p^5P \rightarrow 3s^5S^0$ | 777.4 | 9.14 | 10.74 |
| O I | $3p^3P \rightarrow 3s^3S^0$ | 844.5 | 9.52 | 10.99 |
| OH | $A^2\Sigma^+ \rightarrow X^2\Pi$ | 306 – 319 | - | - |
| NO | $A^2\Sigma^+ \rightarrow X^2\Pi$ | 200 – 330 | - | - |
| N_2 | $C^3\Pi_u \rightarrow B^3\Pi_g$ | 300 – 500 | - | - |
| N_2^+ | $B^2\Sigma_u^+ \rightarrow X^2\Sigma_g^+$ | 350 – 500 | - | - |

Ground state configurations:

He: $1s^2^1S_0$

H: $1s^2S_{1/2}$

O: $1s^22s^22p^4^3P_2$

Angular-resolved emission spectroscopy was performed using the experimental apparatus of Figure 7. The He 706 nm and O 777 nm lines were selected for investigation. By collecting light at angles above the critical angle (for fused silica-air interface the critical angle is 43.4°), one is effectively probing the region close to the plasma-surface interface where the evanescent wave forms. As observed in Figure 14, the intensity of both O and He decreases linearly (in log scale) at angles below the critical angle. At angles above the critical angle, both He and O emissions dropped dramatically (by approximately three orders of magnitude), as expected, but there are still detected. Also, a change in relative intensities is seen at angles above the critical angle with the O emission being more intense probably due to enhanced chemistry near the surface.

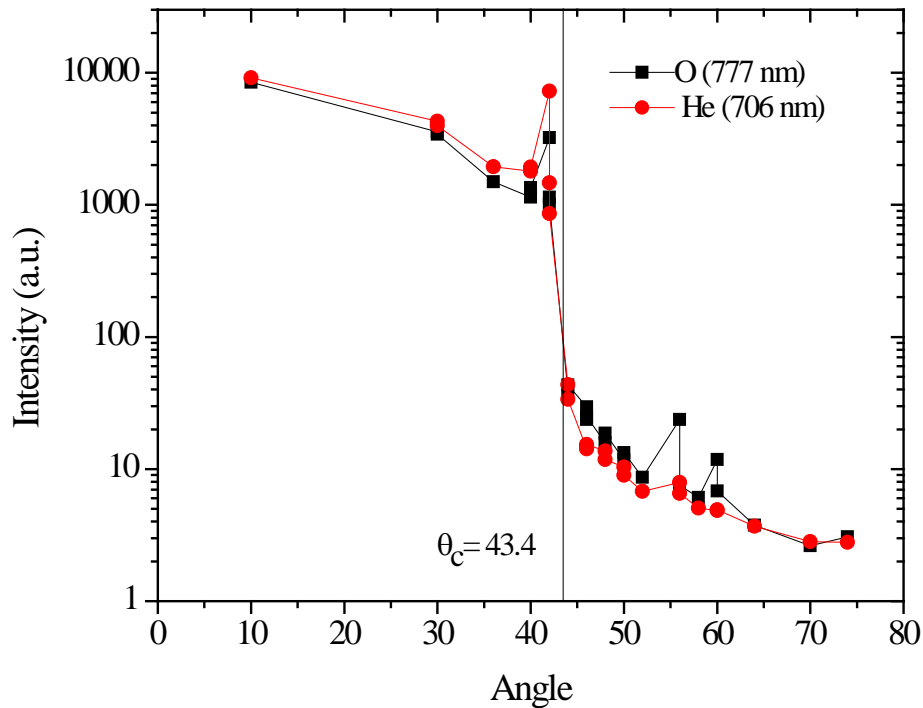


Figure 14 Angular-resolved optical emission spectroscopy.

Unfortunately, subsequent experiments consisting of directing light from a Hg lamp at the surface, led us to conclude that the light collected at angles above the critical angle is probably being detected due to scattering from volume defects and surface scratches of the quartz prism.

4.2 Time-resolved Imaging and Spectroscopy

Plasma current and voltage measurements are shown in Figure 15. The current through the grounded electrode was measured as the voltage drop across a 100 Ω resistor. The voltage applied to the HV electrode is measured using a high voltage probe (1000:1 attenuation) and recorded using a digital oscilloscope. A voltage of ~ 7 kVp-p was applied to ignite the plasma and the current measurements showed two distinct spikes, one during the positive half cycle and the other during the negative half cycle.

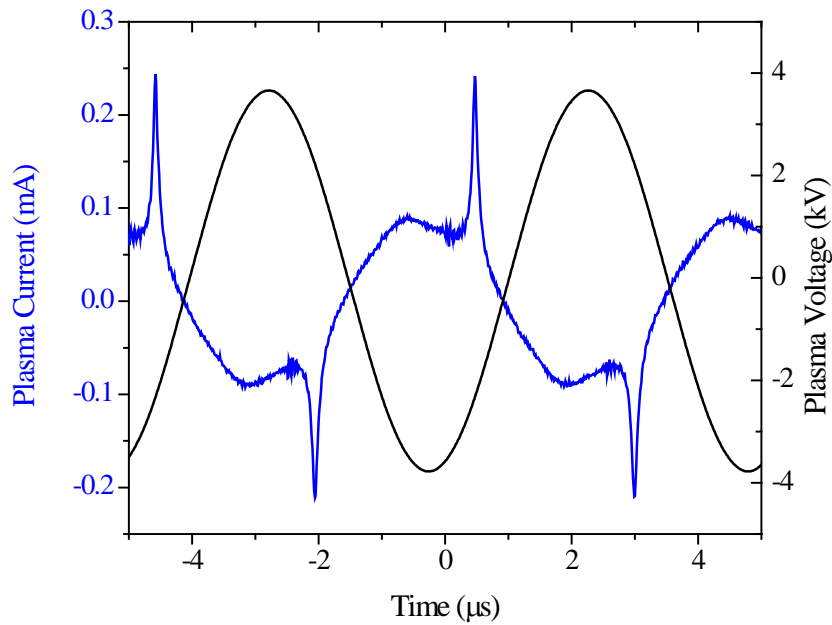


Figure 15 Atmospheric pressure plasma jet voltage-current plot.

The development of the plasma jet was recorded by capturing images along different positions (Figure 16) of the RF period with the ICCD. The resulting images are shown in Figure 17. The plasma jet extends in air only during the positive half cycle. The light intensity reaches two peak values, when the applied voltage is near its maximum and minimum, being considerably more intense during the negative half cycle. Even though a plasma bullet is not very well defined in these images, a transient behavior is evident where the ionization front seems to reach the surface approximately 800 ns after the applied voltage reaches its peak value. This was determined visually when the plasma was more intense near the surface being impinged by the plasma jet.

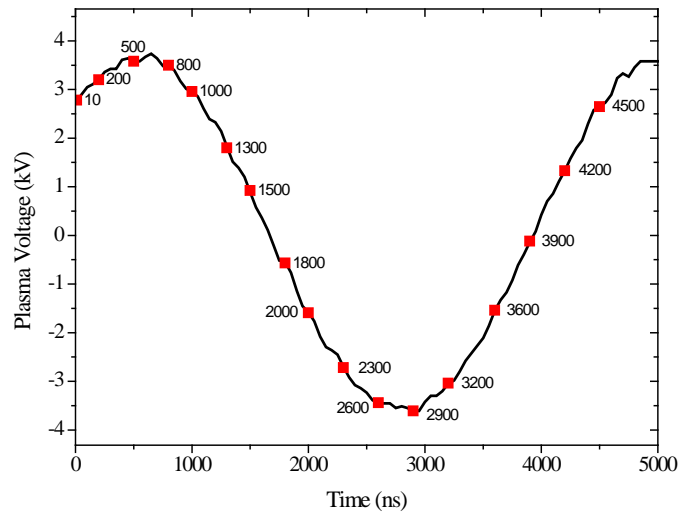
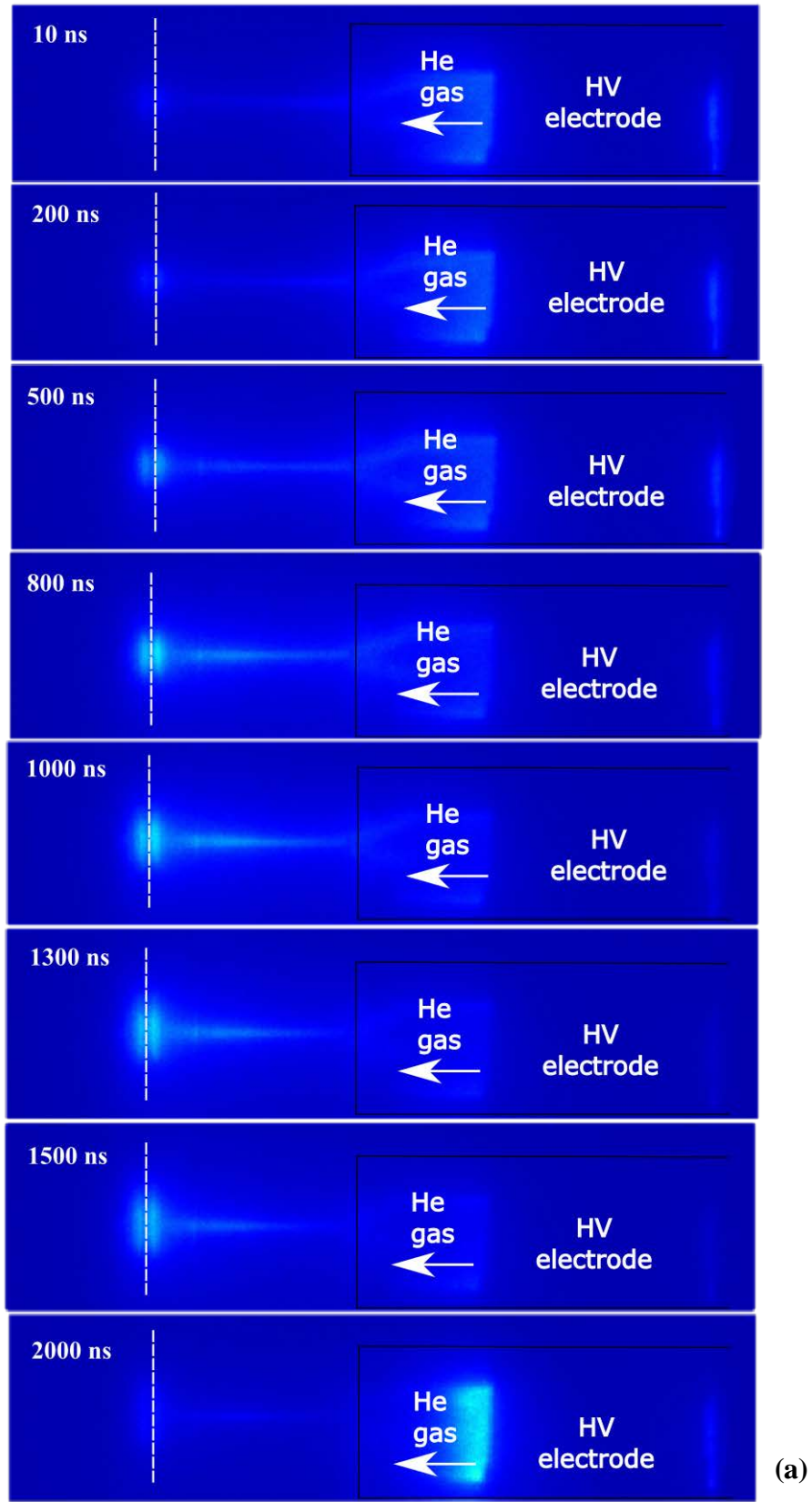


Figure 16 Time along plasma voltage corresponding to when the images of Figure 17 were taken.

During the negative polarity of the voltage, the electric field inside the glass tube is probably stronger since the light intensity is higher. Similar observations were made by Naidis^[13] from simulations of the time resolved light intensity normalized with respect to the N₂ (C –B) emission. Other investigators have also reported that the electric field inside the glass tube is more intense with a negative polarity of the applied voltage,^[8, 47]

hence generating a more intense plasma. During the positive polarity, the electric field inside the tube was low and therefore emission was mostly localized near the head region of the plasma bullet since the N_2 ($C^3\Pi$) lifetime was much smaller than the lifetime of propagation for the bullet. On the contrary, when the electric field was much stronger (i.e., during the negative polarity) the N_2 ($C^3\Pi$) was mostly generated inside the tube and did not propagate much in air. Another possibility, perhaps even more interesting, is that the plasma is behaving similarly to that of Li et al.^[51] where the ionization front propagated in the upstream direction during the negative half-cycle.



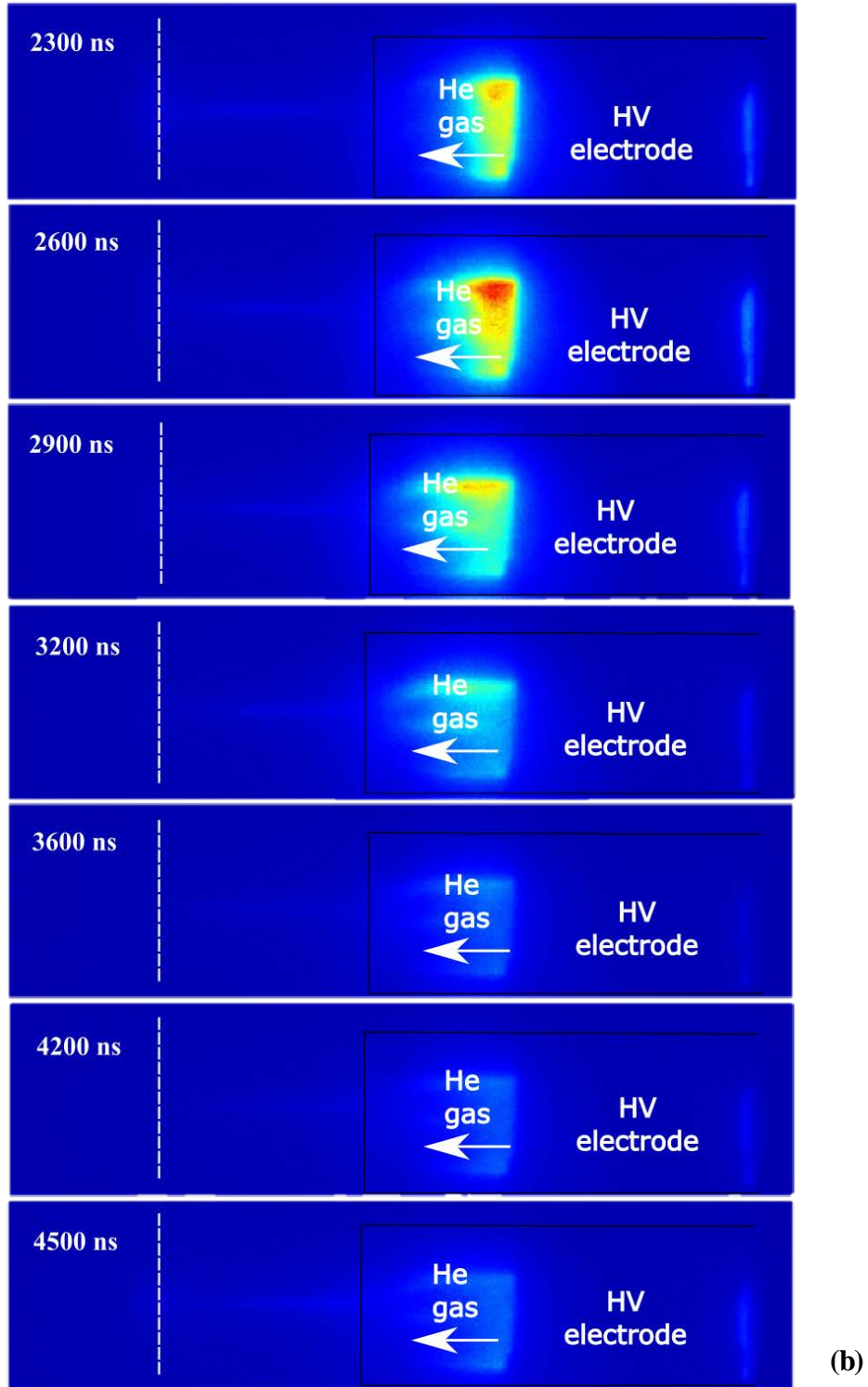


Figure 17 ICCD 10 ns exposure time images (false color) of helium atmospheric pressure plasma jet from (a)10-2000 ns and (b)2300-4500 ns. Corresponding times are shown on the voltage waveform of Figure 16.

Emissions from He (706 nm) and O (777 nm) were time-resolved using the ICCD-spectrometer setup described in section 3.4. By activating the ICCD over 50 ns at different instants with respect to the voltage applied to the plasma, one may be able to understand the origin of the He and O emissions. As shown in Figure 18 (see time with respect to the voltage waveform in Figure 19), the He emission is most intense when the plasma is inside the quartz tube during the negative half of the voltage cycle. This agrees quite well with the images in Figure 17, where the plasma is most intense inside the quartz tube and does not propagate out into open air. On the contrary, during the positive half of the cycle, the He emission is considerably weaker, corresponding to the ionization front propagating in open air. Measurements taken at angles between 10 and 42 degrees (with respect to the jet axis), where photons generated inside the quartz tube cannot reach the optical fiber's field of view, show that He emission was nonexistent during the period when the plasma is confined inside the glass tube. Light collected at angles between 10 degrees and below the critical angle, is coming from a region close to the prism surface as depicted in Figure 20. For these cases, light collected at angles 10° , 20° , and 30° comes from an angle of 15° , 30° , and 77° with respect to the jet's axis.

These results agree with the results of Figure 14 in that the intensity of the He emission drops as a function of angle away from the normal. Emission taken at angles greater than 10 degrees reached a maximum 750 ns after that taken at 0 degrees. This appears to be the time it takes for the ionization front from the discharge to that travel through the air and strike the surface.

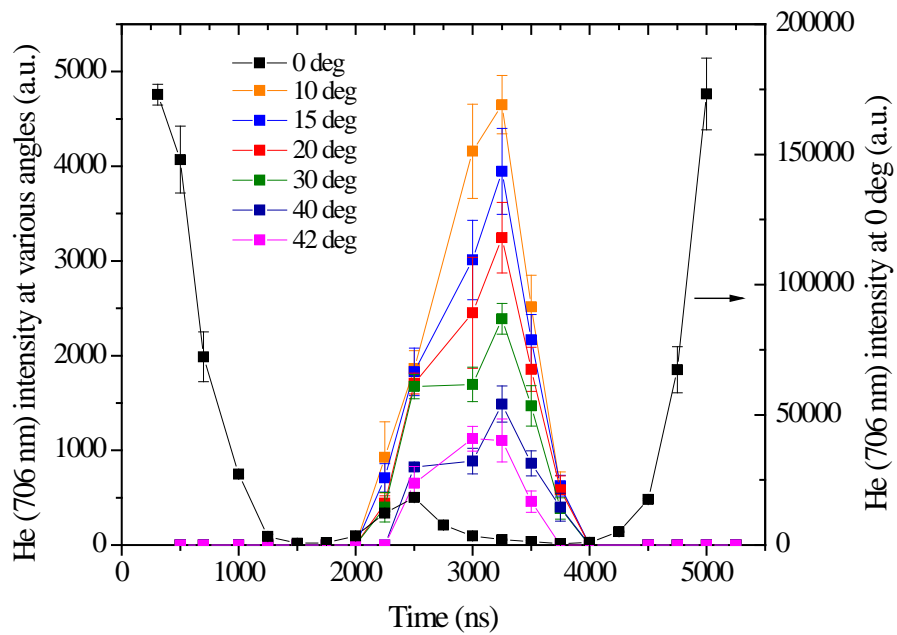


Figure 18 Time-resolved He emission at various angles. Intensities of all but the 0° measurements are indicated by the left y-axis.

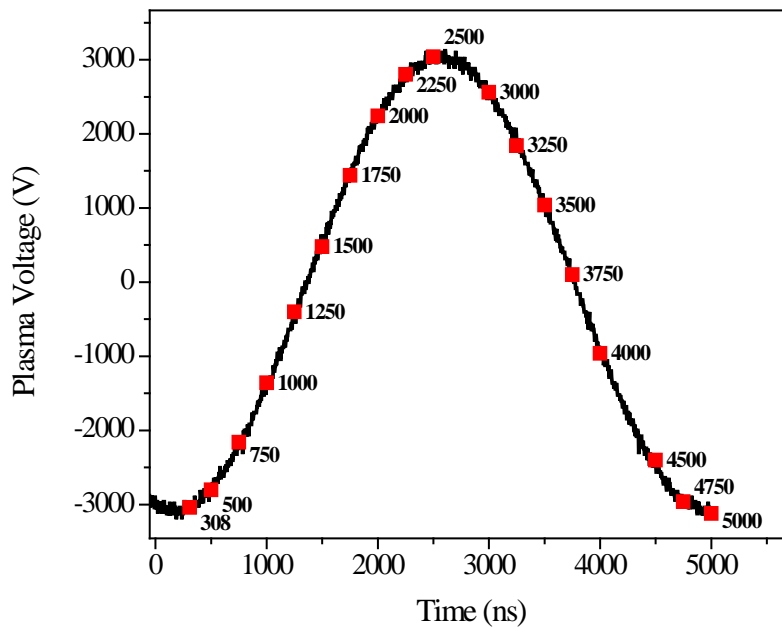


Figure 19 Position in time corresponding to time-resolved emissions.

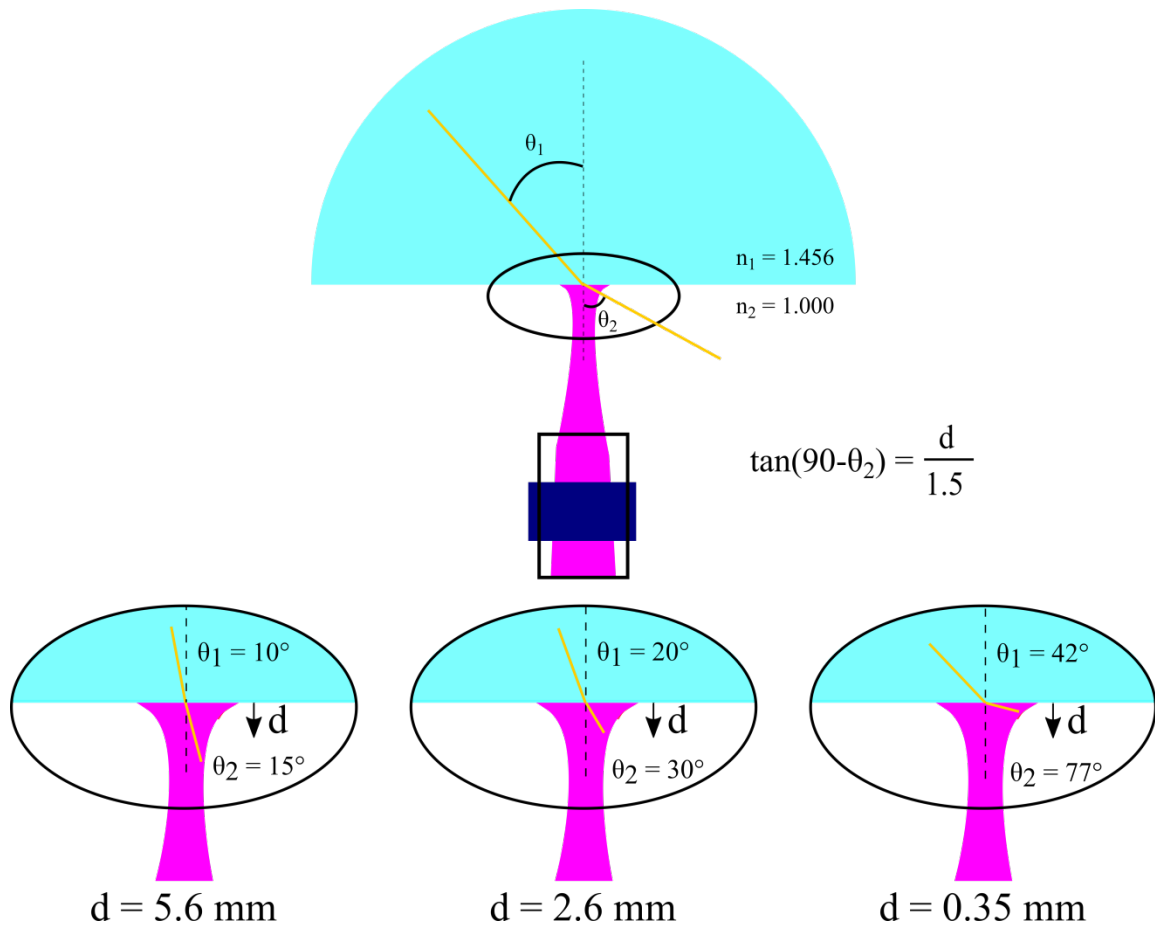


Figure 20 Probing the region close to the prism surface. By collecting OES at 10°, 20°, and 30°, one is probing light from approximately 5.6, 2.6, and 0.35 mm away from the surface.

4.3 UV/VUV to NIR Time-resolved Spectroscopy

High energy VUV photons are of great interest in APPJ for their potential involvement in photochemistry, e.g., photoionization, sterilization, substrate damage, etc. More relevant to this study, they have the ability to excite and/or dissociate species other than He. In addition, they can play a role in surface chemistry induced by atmospheric pressure plasmas. Using the VUV spectrometer and MgF₂ window (Figure 10), several emissions in the VUV region were detected from O, N, H, OH and NO, as shown in Figure 21. The respective transitions and energies are shown in Table 3. Some of these emissions have been reported by others, using a similar setup with He/O₂ plasma^[52] and Ar plasma.^[53] It is evident that the VUV photons detected through open air, and are presumably coming from a region close to the surface of the window.

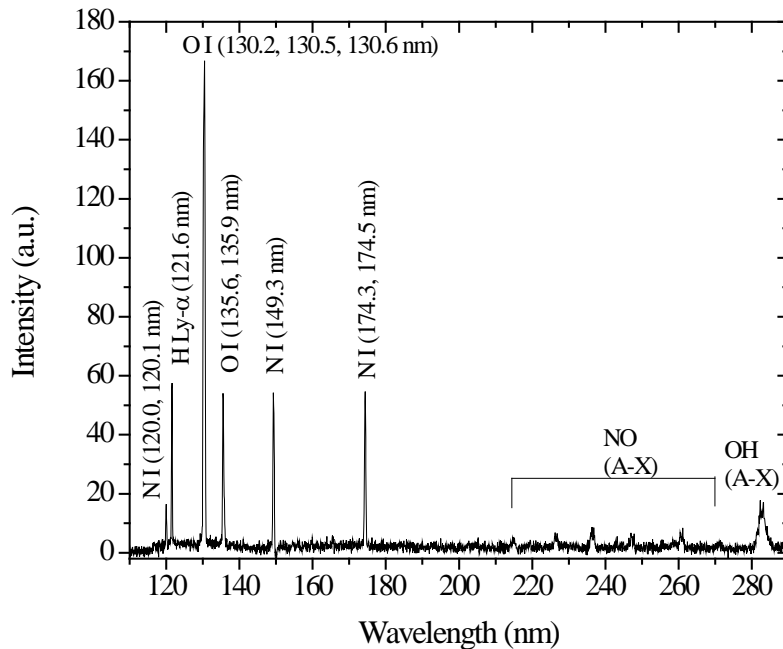


Figure 21 He atmospheric pressure plasma spectrum in the UV-VUV range.

Table 3 Typical emitting species and VUV transitions in He atmospheric pressure plasma jet emerging in air ambient.

| Emitting species | Transition (de-excitation) | λ (nm) | E_{Lower} (eV) | E_{Upper} (eV) |
|------------------|----------------------------------|------------------------|-------------------------|-------------------------|
| N I | $3s^4P \rightarrow 2p^3^4S^0$ | 120.0, 120.1 | 0.00 | 10.23 |
| H Ly- α | $2p^2P^0 \rightarrow 1s^2S$ | 121.6 | 0.00 | 10.20 |
| O I | $3s^3S^0 \rightarrow 2p^4^3P$ | 130.2, 130.5, 130.6 | 0.00 | 9.54 |
| O I | $3s^5S^0 \rightarrow 2p^4^3P$ | 135.6, 135.9 | 0.00, 0.02 | 9.14 |
| N I | $3s^2P \rightarrow 2p^3^2D^0$ | 149.3 | 2.38 | 10.69 |
| N I | $3s^2P \rightarrow 2p^3^2P^0$ | 174.3, 174.5 | 3.67 | 10.69, 10.68 |
| NO | $A^2\Sigma^+ \rightarrow X^2\Pi$ | 200-330 | - | - |
| OH | $A^2\Sigma^+ \rightarrow X^2\Pi$ | 281-288 | - | - |

Ground state configurations:

N: $1s^2 2s^2 2p^3^4S^0_{3/2}$

H: $1s^2S_{1/2}$

O: $1s^2 2s^2 2p^4^3P_2$

Additional experiments were performed with a second MgF₂ window to create an air gap between the windows to investigate how these photons are absorbed by oxygen present in ambient air. Using a movable stage with a precision of 0.01 mm, the gap between the windows was successively increased and the O 130.2 nm and N 149.2 nm emissions were monitored, as shown in Figure 22.

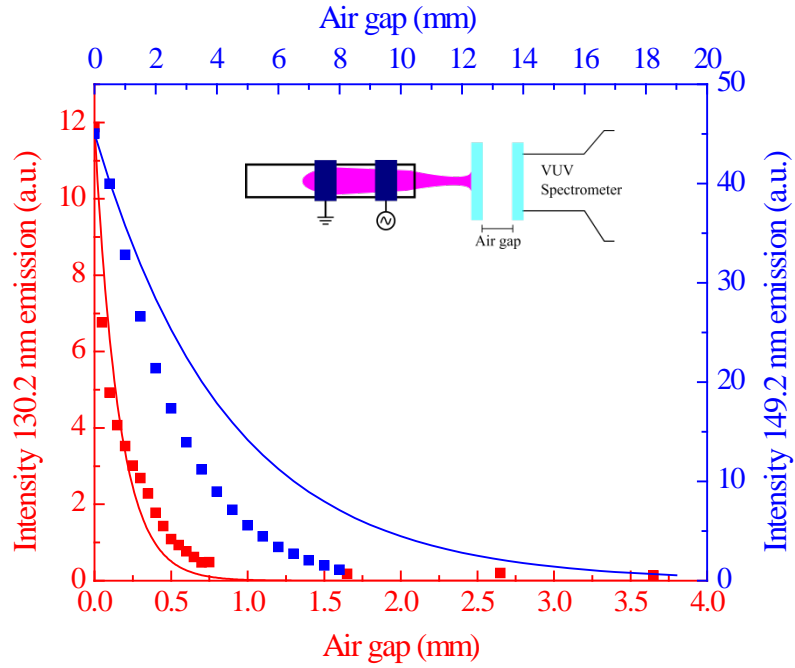


Figure 22 Absorption of O 130.2 nm and N 149.2 VUV photons in air.

Figure 22 shows a fair agreement between the experimental data and the values computed from the Beer-Lambert law

$$I = I_0 \exp(-\alpha pl), \quad (12)$$

where I_0 is the initial intensity recorded when there is no air gap between the windows, α is the absorption coefficient in $\text{cm}^{-1} \text{atm}^{-1}$, p is the pressure of the absorbing medium in atm and l is the path length of the VUV photon in air.

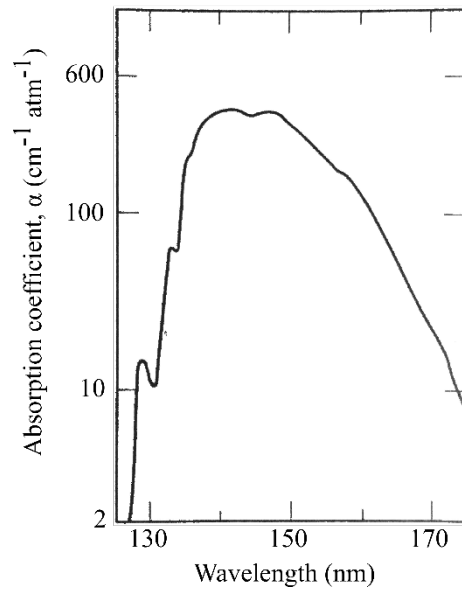


Figure 23 Absorption spectrum of O_2 .^[54]

The deviation from the model for the O emission at distances greater than 2 mm is explained by the fact that at longer distances the amount of light that is able to reach the spectrometer is substantially reduced. Absorption of the 149.2 nm emission agrees better with the Beer-Lambert law since the absorbance coefficient of this wavelength by O_2 is higher than that of 130.2 nm by a factor of almost 30, as shown in Figure 23. Due to the much stronger absorbance of the 149.2 nm line, the measured intensity is already very low at small air gaps to the point that gap sizes larger than 1mm do not make a difference.

To understand better the role that VUV photons can play in photoionization and propagation of atmospheric pressure plasma jets in air, the O I (130.2-130.6 nm) emission was time resolved. The time resolved VUV emission of O I (Figure 24) reached a maximum intensity at the peak voltage of the RF power. However, this emission didn't show a strong modulation, in contrast to the He 706 emission which exhibited two

maxima (Figures 19 and 25) one during the positive phase of the voltage and a more intense peak close to the minimum voltage. O emission from inside the quartz tube, where the plasma is first generated, cannot be attributed to O₂ from surrounding air that diffuses upstream, since the Peclet number is $\gg 1$, i.e., the movement of species is highly advective and dominated by the helium stream. It was concluded that O emission originated in O₂ impurities in the working gas, by positioning the plasma jet at an angle with respect to the MgF₂ window. This prevented any light from the plasma generated inside the quartz tube from being detected by the spectrometer. As expected, the intensity only peaked once (see Figure 24(b)) during the positive phase of the voltage, and dropped to zero for the rest of the RF period.

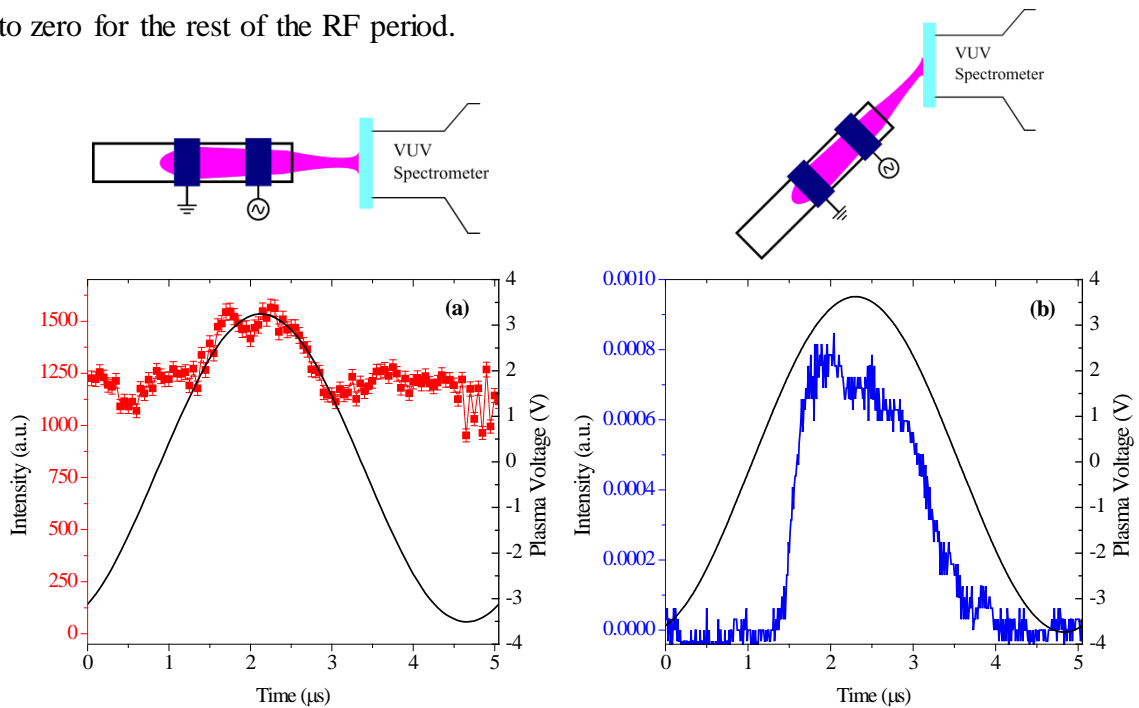


Figure 24 Time resolved O 130.2 nm emission with plasma jet positioned (a) normal to the MgF₂ window and (b) at some angle with respect to the surface.

Similarly to the O 130.2 nm emission, the VUV emissions in the helium plasma were time-resolved (Figure 25) and didn't show strong modulation; more evidence of the presence of O₂ and N₂ impurities in the gas stream.

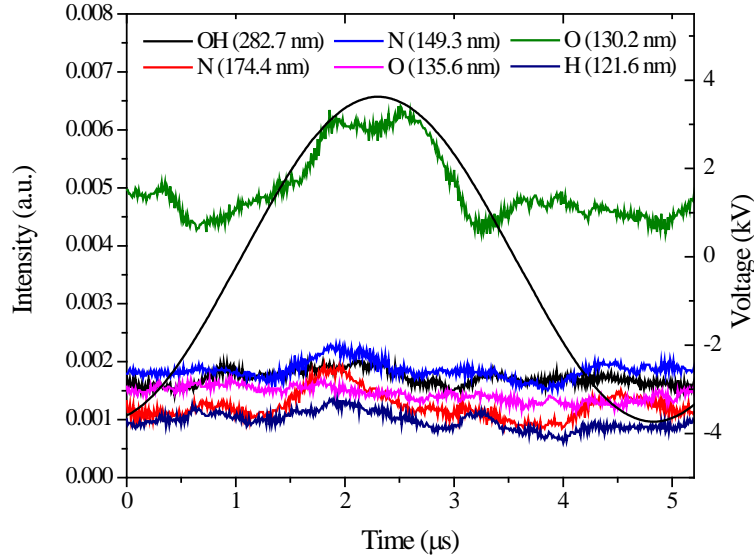
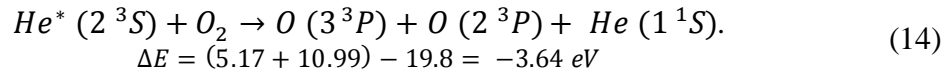
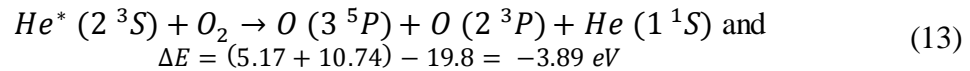


Figure 25 Time resolved VUV emissions.

Time resolved emissions (using the ICCD) of the O 777 nm (Figure 26) and O 844 nm lines didn't show a strong modulation like the He emission. This suggests that these long lived oxygen excited species might arise from any of the following reactions (Penning Ionization) which are thermodynamically favorable; these are:



These long lived metastable states of helium (He*),^[55] responsible for dissociating O₂ (5.17 eV bond energy) and generating excited states of O, are generated by electron

impact on ground state He. These excited states of O (5P and 3P) will decay to $^5S^0$ and $^3S^0$ and lead to the 777 nm and 844 nm emission lines, which are seen in the spectrum. In turn, decay of O ($^3S^0$) to its ground state will liberate 130 nm VUV photons. These same dissociative excitation reactions were also studied by Walsh et al. [56] for a He/O₂ DBD configuration. They determined that collisional excitation of O₂ by helium metastable was significantly more efficient than electron impact dissociative excitation of O₂, electron excitation of O and ion-ion recombination. A similar mechanism is suggested for exciting NO and N which didn't show strong modulation (Figure 25) of the emission. Such excitation reactions can also be driven by the other metastable helium (2^1S) with a slightly higher energy of 20.6 eV.

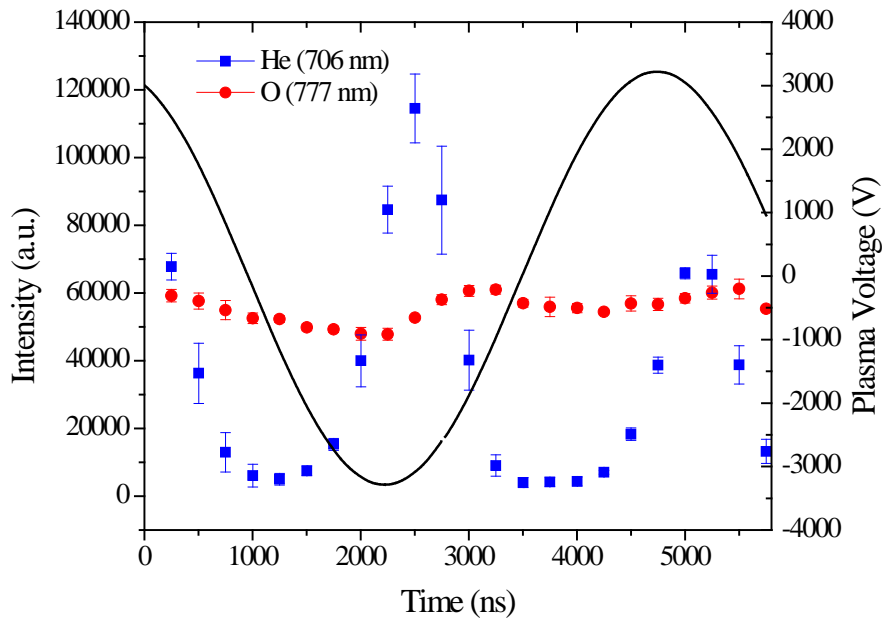
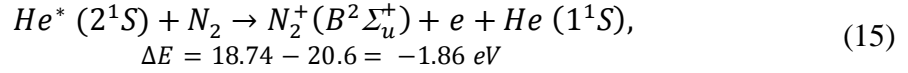
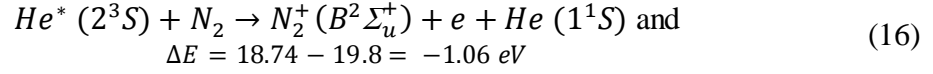
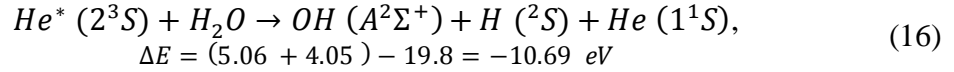


Figure 26 Time-resolved He (706 nm) and O (777 nm) emissions recorded with the ICCD camera.

Similarly to the long lived O, the OH (Figure 27) and N₂⁺ FNS (Figure 28) emissions were not strongly modulated and persisted throughout the applied voltage. This suggests a similar mechanism by which N₂ is excited from its ground state by the following reaction with either one of the helium metastable states such as:



where the excess energy of 1.06 eV and 1.86 eV is easily carried away by the electron. Similarly, the OH emission has its origin in the reaction between He* and H₂O (dissociation energy of 5.06 eV) to form OH (A²Σ⁺) and the ground state of hydrogen,



where the excess energy of 10.69 eV goes mainly into translational energy after the dissociation of H-OH or exciting H into one of its energetic states.

Finally, excitation of hydrogen (H Lyman-α, 121.6 nm and H Balmer-α, 656.3 nm) persisted throughout the RF period, as shown in Figure 25 and time-resolved spectra in Figure 28, consistent with He* being responsible for dissociation of water molecules and producing OH (A²Σ⁺) and H, with one or the other (, or both – this depends on whether reaction 16 with ¹S or ³S has enough energy to do this) in an excited state.

Contrary to any other time-resolved emission, the N₂ (C→B, 337 nm) emission from the SPS, shown in Figure 27, peaked only once during the RF period. This implies that a different mechanism, electron impact ionization, is responsible for the presence of

the SPS. This excited state of N_2 ($C^3\Pi_u$) has a higher probability of being reached by electron impact energy transfer compared to the higher energy needed for the FNS since it requires electrons with energies of at least 11.05 eV. This is supported by the fact that if any of the helium metastable were to be responsible for exciting N_2 into N_2 ($C^3\Pi_u$), there would be an excess amount of energy of approximately 8.75 or 9.55 eV; too much energy to go into translational or vibrational energy.

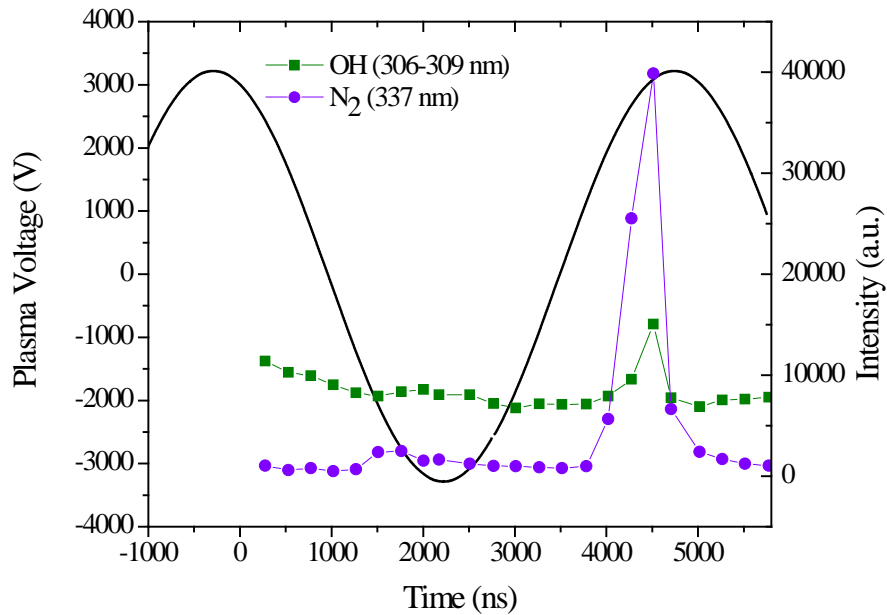


Figure 27 Time resolved OH (306-309 nm) and N_2 SPS (337 nm) emissions recorded with the ICCD camera.

Assuming that the rise in emission of N_2 (337 nm) in Figure 27 comes from electron impact excitation of N_2 near the surface of the prism, the rate of drop in intensity of approximately 500 ns should correspond to the drop in electron density (not measured in our plasma). If this is the case, then the N_2 SPS must be predominantly found outside the quartz tube discharge when the ionization front moves towards the prism. Hence, time

resolved observations of the C-B system at angles above 10 degrees, with the near-absence of this emission inside the quartz tube, should confirm this.

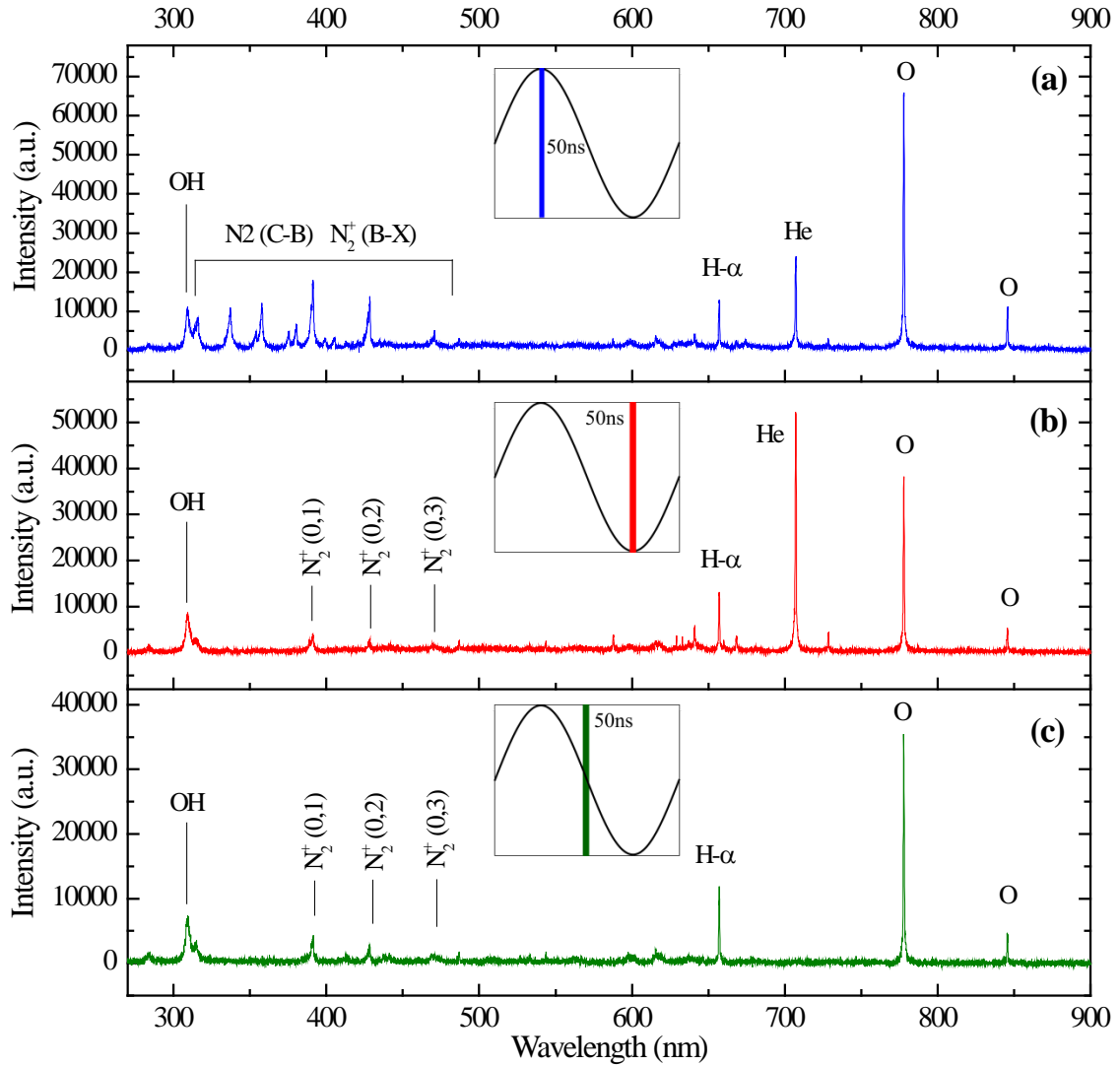


Figure 28 Helium atmospheric pressure plasma spectrum (a) at the maximum of the applied voltage, (b) the minimum of the applied, and (c) at the zero crossing of the applied voltage.

Chapter 5: Summary and Conclusions

The study of non-equilibrium (cold) atmospheric pressure plasmas jets (APPJs) has received much attention in recent years. These types of plasmas not only have a low gas temperature but are also able to transport reactive species like NO, OH, O₃, O and VUV photons, to a localized area, which makes such devices good candidates for the rapidly expanding field of plasma medicine. It is vital to have a detailed understanding of plasma physics and chemistry, particularly near the treated surface, due to the complexity of these plasmas. Additionally, the role that VUV photons play in these plasmas has not been given enough attention thus far.

In this research, optical emission spectroscopy was performed to study helium APPJs. To probe light from the region in the last 100 nm from the surface impinged by the plasma jet, a technique based on evanescent wave optical emission spectroscopy was developed. However, spurious light scattered from inclusions and surface scratches in the optical element prevented the full implementation of this technique. High-speed imaging and time-resolved VUV and UV-IR spectroscopy were implemented to study the time evolution of the plasma and further understand the origin of different emissions. It was determined that excited metastable helium plays an important role and is highly responsible for plasma penning ionization. The energy from these metastable states is mostly transferred to other gas impurities or admixtures such as N₂, H₂O or O₂ that might be present in the helium stream or that can diffuse into the plasma jet. In fact, it acts as a form of energy reservoir during the period when the plasma doesn't extend in air by generating a partially ionized gas that helps sustain the plasma with assistance from VUV

high energy photons. This gave rise to N_2 , OH, and O emissions that are not highly modulated (except for N_2 (C-B)) like the He emission.

Further investigation of OH, O and N_2 emissions will require the use of higher purity helium working gas. Also, introducing additives to the ambient air surrounding the plasma jet to obtain higher or lower concentration of N_2 , water vapor or oxygen should reinforce the importance of the helium metastable. Additionally, determination of electron density and its decay rate along the plasma plume using the Stark broadening of the hydrogen Balmer series atomic lines should give insight on the excitation of N_2 , by electron impact, near the prism surface.

References

- [1] C. Tendero, C. Tixier, P. Tristant, J. Desmaison, and P. Leprince, “Atmospheric pressure plasmas: A review,” *Spectrochim. Acta - Part B At. Spectrosc.*, vol. 61, no. 1, pp. 2–30, 2006.
- [2] K. H. Schoenbach and K. Becker, “20 Years of Microplasma Research: a Status Report,” *Eur. Phys. J. D*, vol. 70, no. 2, p. 29, 2016.
- [3] X. Lu, G. V. Naidis, M. Laroussi, and K. Ostrikov, “Guided ionization waves: Theory and experiments,” *Phys. Rep.*, vol. 540, no. 3, pp. 123–166, 2014.
- [4] Y. P. Raizer, *Gas Discharge Physics*. Springer-Verlag Berlin Heidelberg, 1991.
- [5] J. Ehlbeck, U. Schnabel, and M. Polak, “Low temperature atmospheric pressure plasma sources for microbial decontamination,” *J. Phys. D ...*, vol. 44, pp. 453–459, 2011.
- [6] F. C. Francis, “Introduction to Plasma Physics and Controlled Fusion,” *Plasma Phys.*, 1984.
- [7] N. Y. Babaeva and G. V. Naidis, “Dynamics of positive and negative streamers in air in weak uniform electric fields,” *IEEE Trans. Plasma Sci.*, vol. 25, no. 2, pp. 375–379, 1997.
- [8] H. Conrads and M. Schmidt, “Plasma generation and plasma sources,” *Plasma Sources Sci. Technol.*, vol. 9, no. 4, pp. 441–454, 2000.
- [9] F. Alexander and K. Lawrence A., *Plasma Physics and Engineering*. CRC Press, 2011.
- [10] A. Fridman, A. Chirokov, and A. Gutsol, “Non-thermal atmospheric pressure discharges,” *J. Phys. D. Appl. Phys.*, vol. 38, no. 2, p. R1, 2005.

- [11] N. S. J. Braithwaite, "Introduction to gas discharges," *Plasma Sources Sci. Technol.*, vol. 9, pp. 517–527, 2000.
- [12] R. M. Sankaran, *Plasma processing of nanomaterials*. CRC Press, 2011.
- [13] G. V. Naidis, "Simulation of streamers propagating along helium jets in ambient air: Polarity-induced effects," *Appl. Phys. Lett.*, vol. 98, no. 14, pp. 3–5, 2011.
- [14] T. L. Ni, F. Ding, X. D. Zhu, X. H. Wen, and H. Y. Zhou, "Cold microplasma plume produced by a compact and flexible generator at atmospheric pressure," *Appl. Phys. Lett.*, vol. 92, no. 24, pp. 9–12, 2008.
- [15] Y. C. Hong, H. S. Uhm, and W. J. Yi, "Atmospheric pressure nitrogen plasma jet: Observation of striated multilayer discharge patterns," *Appl. Phys. Lett.*, vol. 93, no. 5, pp. 5–8, 2008.
- [16] Y. C. Hong, W. S. Kang, Y. B. Hong, W. J. Yi, and H. S. Uhm, "Atmospheric pressure air-plasma jet evolved from microdischarges: Eradication of *E. coli* with the jet," *Phys. Plasmas*, vol. 16, no. 12, pp. 1–6, 2009.
- [17] Z. Machala, E. Marode, C. O. Laux, and C. H. Kruger, "DC Glow Discharges in Atmospheric Pressure Air," *J. Adv. Oxid. Technol.*, vol. 7, no. 2, pp. 3–7, 2004.
- [18] K. G. Kostov, M. Machida, and V. Prysiaznyi, "Generation of Cold Argon Plasma Jet at the End of Flexible Plastic Tube," *Plasma Sources Sci. Technol.*, vol. 24, 2012.
- [19] J. Heinlin, G. Morfill, M. Landthaler, W. Stolz, G. Isbary, J. L. Zimmermann, T. Shimizu, and S. Karrer, "Plasma-Medizin: Anwendungsmöglichkeiten in der Dermatologie," *JDDG - J. Ger. Soc. Dermatology*, vol. 8, no. 12, pp. 968–977, 2010.

- [20] M. Teschke, J. Kedzierski, E. G. Finantu-Dinu, D. Korzec, and J. Engemann, "High-speed photographs of a dielectric barrier atmospheric pressure plasma jet," *IEEE Trans. Plasma Sci.*, vol. 33, no. 2, pp. 310–311, 2005.
- [21] X. Lu, M. Laroussi, and V. Puech, "On atmospheric-pressure non-equilibrium plasma jets and plasma bullets," *Plasma Sources Science and Technology*, vol. 21, no. 3, p. 034005, 2012.
- [22] I. M. Lagarkov, A. N., & Rutkevick, "Ionization Waves in Electrical Breakdown of Gases," Springer New York, 1994.
- [23] S. Hofmann, A. Sobota, and P. Bruggeman, "Transitions between and control of guided and branching streamers in dc nanosecond pulsed excited plasma jets," *IEEE Trans. Plasma Sci.*, vol. 40, no. 11 PART1, pp. 2888–2899, 2012.
- [24] K. Kelly-Wintenber, T. C. Montie, C. Brickman, J. R. Roth, a K. Carr, K. Sorge, L. C. Wadsworth, and P. P. Tsai, "Room temperature sterilization of surfaces and fabrics with a one atmosphere uniform glow discharge plasma.," *J. Ind. Microbiol. Biotechnol.*, vol. 20, no. 1, pp. 69–74, 1998.
- [25] M. Keidar, A. Shashurin, O. Volotskova, M. Ann Stepp, P. Srinivasan, A. Sandler, and B. Trink, "Cold atmospheric plasma in cancer therapy," *Phys. Plasmas*, vol. 20, no. 5, pp. 0–8, 2013.
- [26] D. B. Graves, "The emerging role of reactive oxygen and nitrogen species in redox biology and some implications for plasma applications to medicine and biology," *J. Phys. D. Appl. Phys.*, vol. 45, no. 26, p. 263001, 2012.
- [27] A. I. Wu, Defeng, & Cederbaum, "Alcohol, oxidative stress, and free radical damage," *Alcohol Res. Heal.*, vol. 27, pp. 277–284, 2003.

- [28] K. P. Arjunan, V. K. Sharma, and S. Ptasinska, "Effects of atmospheric pressure plasmas on isolated and cellular DNA—a review," *Int. J. Mol. Sci.*, vol. 16, no. 2, pp. 2971–3016, 2015.
- [29] Q. Li, J. T. Li, W. C. Zhu, X. M. Zhu, and Y. K. Pu, "Effects of gas flow rate on the length of atmospheric pressure nonequilibrium plasma jets," *Appl. Phys. Lett.*, vol. 95, no. 14, 2009.
- [30] N. Jiang, J. Yang, F. He, and Z. Cao, "Interplay of discharge and gas flow in atmospheric pressure plasma jets," *J. Appl. Phys.*, vol. 109, no. 9, pp. 1–6, 2011.
- [31] E. Robert, V. Sarron, T. Darny, D. Riès, S. Dozias, J. Fontane, L. Joly, and J.-M. Pouvesle, "Rare gas flow structuration in plasma jet experiments," *Plasma Sources Sci. Technol.*, vol. 23, no. 1, p. 012003, 2014.
- [32] W. C. Zhu, Q. Li, X.-M. Zhu, and Y. K. Pu, "Characteristics of atmospheric pressure plasma jets emerging into ambient air and helium," *J. Phys. D. Appl. Phys.*, vol. 42, no. 20, p. 202002, 2009.
- [33] A. Schutze, J. Y. Jeong, S. E. Babayan, J. Park, G. S. Selwyn, and R. F. Hicks, "The atmospheric-pressure plasma jet: a review and comparison to other plasma sources," *Plasma Sci. IEEE Trans.*, vol. 26, no. 6, pp. 1685–1694, 1998.
- [34] H. R. Griem, "Spectral Line Broadening by Plasmas," New York: Academic, 1974.
- [35] Q. Wang, I. Koleva, V. M. Donnelly, and D. J. Economou, "Spatially resolved diagnostics of an atmospheric pressure direct current helium microplasma," *J. Phys. D. Appl. Phys.*, vol. 38, no. 11, pp. 1690–1697, 2005.

- [36] A. Y. Nikiforov, C. Leys, M. A. Gonzalez, and J. L. Walsh, "Electron density measurement in atmospheric pressure plasma jets: Stark broadening of hydrogenated and non-hydrogenated lines," *Plasma Sources Sci. Technol.*, vol. 24, no. 3, p. 034001, 2015.
- [37] H. Akatsuka, "Progresses in Experimental Study of N₂ Plasma Diagnostics by Optical Emission Spectroscopy," 2008.
- [38] S. Koike, T. Sakamoto, H. Kobori, H. Matsuura, and H. Akatsuka, "Spectroscopic study on vibrational nonequilibrium of a microwave discharge nitrogen plasma," *Japanese J. Appl. Physics, Part 1 Regul. Pap. Short Notes Rev. Pap.*, vol. 43, no. 8 A, pp. 5550–5557, 2004.
- [39] Y. Chen, S. Varma, a York, and H. M. Milchberg, "Measurement of rotational wavepacket revivals in H₂, D₂, N₂, O₂, and N₂O," vol. 15, no. 18, pp. 192–194, 2007.
- [40] S. Schneider, J. W. Lackmann, F. Narberhaus, J. E. Bandow, B. Denis, and J. Benedikt, "Separation of VUV/UV photons and reactive particles in the effluent of a He/O₂ atmospheric pressure plasma jet," *J. Phys. D. Appl. Phys.*, vol. 44, no. 37, p. 379501, 2011.
- [41] S. Schneider, J. W. Lackmann, D. Ellerweg, B. Denis, F. Narberhaus, J. E. Bandow, and J. Benedikt, "The role of VUV radiation in the inactivation of bacteria with an atmospheric pressure plasma jet," *Plasma Process. Polym.*, vol. 9, no. 6, pp. 561–568, 2012.

- [42] M. Gu, J. B. Haumonte, Y. Micheau, J. W. M. Chon, and X. Gan, “Laser trapping and manipulation under focused evanescent wave illumination,” *Appl. Phys. Lett.*, vol. 84, no. 21, pp. 4236–4238, 2004.
- [43] P. Taylor, A. I. Lvovsky, and A. I. Lvovsky, “Encyclopedia of Optical Engineering Fresnel Equations Fresnel Equations,” no. August, pp. 37–41, 2013.
- [44] J. S. Guasto, P. Huang, and K. S. Breuer, “Evanescent Wave Illumination,” *Encycl. Micro- Nano-fluidics*, pp. 638–644, 2008.
- [45] C. K. Carniglia, L. Mandel, and K. H. Drexhage, “Absorption and Emission of Evanescent Photons,” *Journal of the Optical Society of America*, vol. 62, no. 4. p. 479, 1972.
- [46] T. Funatsu, Y. Harada, and M. Tokunaga, “Imaging of Single Fluorescent Molecules and Individual Atp Turnovers By Single Myosin Molecules in Aqueous-Solution,” *Nature*, vol. 374, no. 6522. pp. 555–559, 1995.
- [47] X. Lu, M. Laroussi, and V. Puech, “On atmospheric-pressure non-equilibrium plasma jets and plasma bullets,” *Plasma Sources Sci. Technol.*, vol. 21, no. 3, p. 034005, 2012.
- [48] Princeton Instruments, “PI-MAX Camera Manual,” Roper Scientific, Inc, New Jersey, 2002.
- [49] S. Svanberg, "Atomic and Molecular Spectroscopy: Basic Aspects and Practical Applications," New York: Springer-Verlag Berlin Heidelberg, 1992.
- [50] A. Luque, V. Ratushnaya, and U. Ebert, “Positive and negative streamers in ambient air: modeling evolution and velocities,” *J. Phys. D Appl. Phys.*, vol. 41, p. 18, 2008.

- [51] X. C. Li, P. P. Zhang, P. Y. Jia, J. Y. Chen, W. T. Bao, and L. F. Dong, "Dynamics of Atmospheric Pressure Plasma Plumes in the Downstream and Upstream Regions," *Plasma Process. Polym.*, p. n/a–n/a, 2016.
- [52] V. Schulz-Von Der Gathen, V. Buck, T. Gans, N. Knake, K. Niemi, S. Reuter, L. Schaper, and J. Winter, "Optical diagnostics of micro discharge jets," *Contrib. to Plasma Phys.*, vol. 47, no. 7, pp. 510–519, 2007.
- [53] R. Brandenburg, H. Lange, T. von Woedtke, M. Stieber, E. Kindel, J. Ehlbeck, and K.-D. Weltmann, "Antimicrobial Effects of {UV} and {VUV} Radiation of Nonthermal Plasma Jets," *IEEE Trans. Plasma Sci.*, vol. 37, no. 6, pp. 877–883, 2009.
- [54] J. N. Calvert, Jack G., & Pitts, "Photochemistry," New York: John Wiley & Sons, Inc., 1966.
- [55] K. Niemi, J. Waskoenig, N. Sadeghi, T. Gans, and D. O'Connell, "The role of helium metastable states in radio-frequency driven helium-oxygen atmospheric pressure plasma jets: measurement and numerical simulation," *Plasma Sources Sci. Technol.*, vol. 20, p. 055005, 2011.
- [56] J. L. Walsh, D. X. Liu, F. Iza, M. Z. Rong, and M. G. Kong, "Contrasting characteristics of sub-microsecond pulsed atmospheric air and atmospheric pressure helium–oxygen glow discharges," *J. Phys. D. Appl. Phys.*, vol. 43, no. 3, p. 032001, 2010.

Appendix

The following spectra (Figures 29-30) contain all the typical emissions found in a helium atmospheric pressure plasma jet emerging in air ambient. Detailed identification of all peaks including the N_2 Second Positive System ($C^3\Pi_u \rightarrow B^3\Pi_g$) and N_2^+ First Negative System ($B^2\Sigma_u^+ \rightarrow X^2\Sigma_g^+$) are shown.

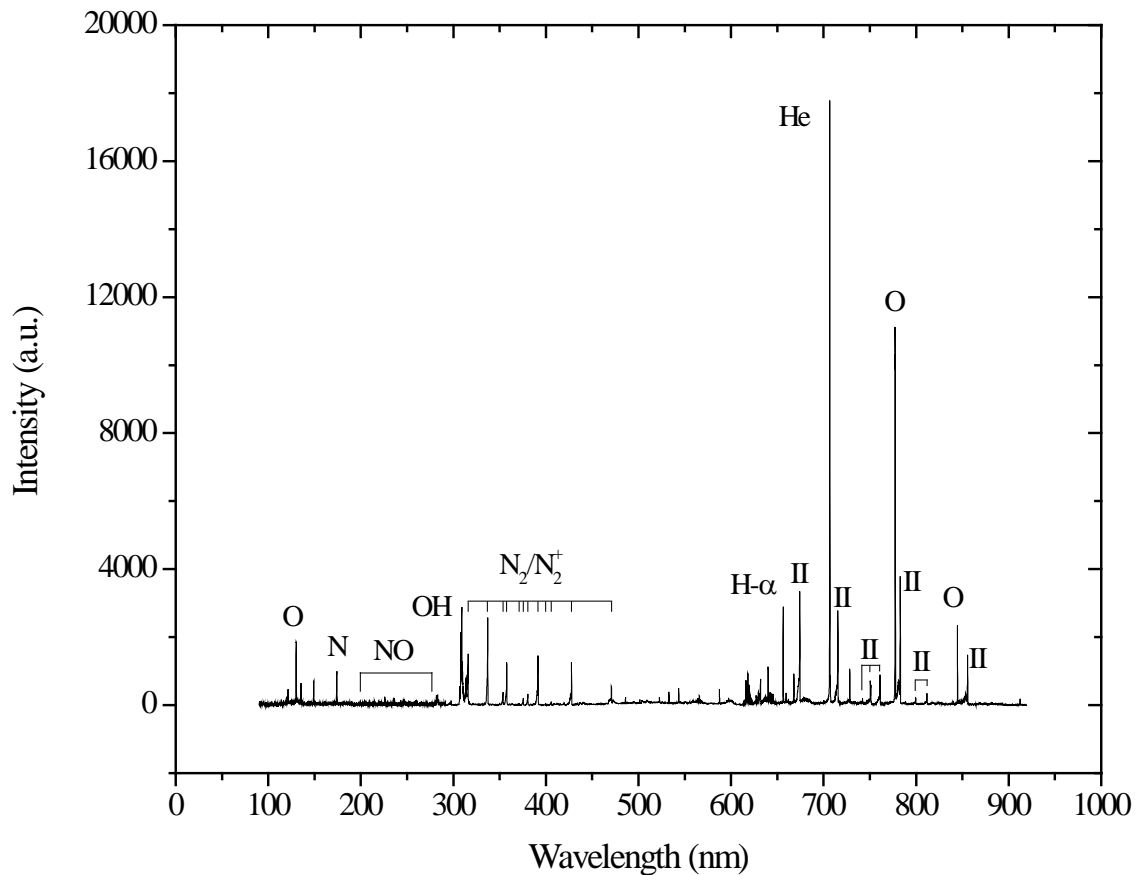


Figure 29 Typical He atmospheric pressure plasma spectrum from 100 nm to 900 nm. Peaks marked with II are those from second-order diffraction.

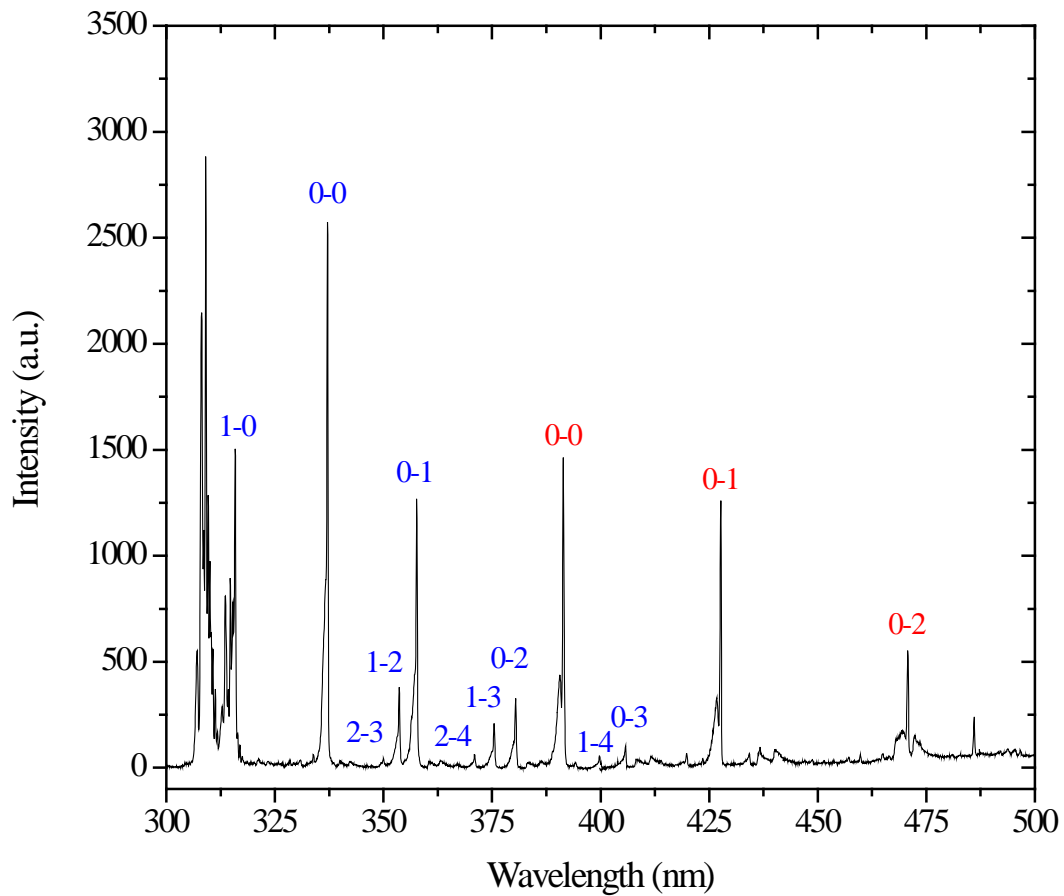


Figure 30 Typical emission spectrum, exhibiting both N_2 (blue) and N_2^+ (red) with corresponding vibrational quantum numbers $v'-v''$.

Table 4 N_2 and N_2^+ transitions in He atmospheric pressure plasma jet.

| Emitting species | Transition $v'-v''$ | λ (nm) | Emitting species | Transition $v'-v''$ | λ (nm) |
|------------------|---------------------|----------------|------------------|---------------------|----------------|
| N_2 | 1-0 | 315.8 | N_2 | 0-2 | 380.4 |
| N_2 | 0-0 | 337.0 | N_2 | 1-4 | 399.7 |
| N_2 | 2-3 | 349.9 | N_2 | 0-3 | 405.8 |
| N_2 | 1-2 | 353.6 | N_2^+ | 0-0 | 391.4 |
| N_2 | 0-1 | 357.6 | N_2^+ | 0-1 | 427.8 |
| N_2 | 2-4 | 370.9 | N_2^+ | 0-2 | 470.9 |
| N_2 | 1-3 | 375.4 | | | |